Remote Sensing of Environment 269 (2022) 112805

Contents lists available at ScienceDirect

Remote Sensing of Environment

journal homepage: www.elsevier.com/locate/rse

CryoSat-2 interferometric mode calibration and validation: A case study from the Austfonna ice cap, Svalbard

Ashley Morris [a,1,*], Geir Moholdt [a], Laurence Gray [b], Thomas Vikhamar Schuler [c,d], Trond Eiken [c]

[a] Norwegian Polar Institute, Fram Centre, 9296 Tromsø, Norway
[b] Department of Geography, Environment and Geomatics, University of Ottawa, Ottawa, ON K1N 6N5, Canada
[c] Department of Geosciences, University of Oslo, 0316 Oslo, Norway
[d] Department of Arctic Geophysics, University Centre in Svalbard, UNIS, P.O. Box 156, N-9171 Longyearbyen, Norway

ARTICLE INFO

Edited by Dr. Menghua Wang

Keywords:
CryoSat-2
SARIn
Radar altimetry
Calibration
Validation
Austfonna

ABSTRACT

Satellite radar altimetry is widely used to measure glacier and ice sheet elevation changes, but can suffer from uncertainties related to geolocation and signal penetration. The unique capabilities of ESA's CryoSat-2 allow for accurate geolocation but impacts from signal penetration persist. This study uses surface elevations from Global Navigation Satellite System and airborne laser transects over the Austfonna ice cap, Svalbard, to measure the elevation bias of CryoSat-2 Point-of-closest-approach (POCA) and swath points, and to provide validation for $\frac{dh}{dt}$ estimates derived through the application of a least-squares plane-fit algorithm to these data. The mean elevation bias of swath points varies between 1 and 1.5 m of penetration, which is close to observed winter snow depths. Histograms of POCA elevation bias for the applied leading-edge retracker peak near the surface, with a distribution skewed towards the sub-surface. At the onset of surface melt, surface scattering dominates backscatter, and penetration reduces. This results in spurious peaks in derived elevation and mass change time series. In spite of this seasonal variability in elevation bias, the validation $\frac{dh}{dt}$ dataset demonstrates that the CryoSat-2 $\frac{dh}{dt}$ estimates are robust on multi-year timescales. The transition from volume to surface scattering suggests the potential to estimate yearly snowpack thickness.

1. Introduction

Satellite radar altimetry is frequently used to measure surface elevations of the global ocean, sea ice, and land ice. In glaciology it provides a multi-decadal dataset with which to map elevation and elevation change of the Greenland and Antarctic ice sheets (Shepherd et al., 2012, 2018, 2020; Helm et al., 2014; Sandberg Sørensen et al., 2018; Zwally et al., 2005), as well as the thickness change of Antarctic ice shelves (Paolo et al., 2015; Zwally et al., 2005). The applicability of radar altimetry to smaller ice masses such as polar and subpolar glaciers, ice caps and icefields has increased with the advent of spaceborne interferometric synthetic aperture radar altimetry since the 2010 launch of CryoSat-2 (Morris et al., 2020; Gray et al., 2015; Foresta et al., 2016, 2018; McMillan et al., 2014; Noël et al., 2018; Jakob et al., 2021; Tepes et al., 2021, 2021). Thorough calibration and validation studies are necessary to quantify biases, ensuring intercomparability of elevations and rates of elevation change derived from data from different radar and laser altimetry satellites. This section gives an overview of the measurement principle and sources of error, and discusses previous CryoSat-2 calibration and validation studies.

A conventional satellite radar altimeter emits a pulse train and measures the two-way travel time to the Earth's surface. Initial echoes are received from a small area at the minimum distance between the satellite and the Earth's surface, the point of closest approach (POCA). As time goes on, an increasing area of the surface around the POCA is illuminated, the pulse eventually illuminating a subsatellite footprint with a diameter of several kilometres. At the end of the pulse, a decreasing ring of the surface is illuminated. Plotting backscatter to the satellite against time yields a 'waveform' from which the two-way travel time to the POCA can be extracted. The backscatter will initially increase as the POCA is illuminated, and will continue to increase as the area of the surface illuminated increases, forming the steep 'leading edge' of the waveform. The peak of the waveform occurs at maximum surface illumination and is followed by a 'trailing edge' as the decreasing ring of the

* Corresponding author.
E-mail address: richard.ashley.morris@gmail.com (A. Morris).
[1] Present address: Department of Earth and Space Sciences, University of Washington, Seattle, WA 98195, United States of America.

https://doi.org/10.1016/j.rse.2021.112805
Received 8 February 2021; Received in revised form 12 October 2021; Accepted 12 November 2021
Available online 24 November 2021

surface is illuminated and backscatter gradually decreases. This idealised waveform shape will be modified in complex terrain. The time delay to an area representative of the POCA is derived from the waveform using a 'retracker' algorithm.

Where the subsatellite topography is flat, such as the oceans, sea ice, and the interior of the ice sheets, the POCA will be located at satellite nadir. However, where subsatellite topography is sloping, the POCA will be displaced upslope. *A priori* knowledge of subsatellite topography is then necessary to convert the delay time to a geocoded elevation estimate. This has been shown to introduce considerable errors, even for seemingly insignificant slopes (Hurkmans et al., 2012; Schröder et al., 2017; Brenner et al., 1983), and is particularly problematical in rapidly changing terrain such as retreating tidewater glaciers and surging glaciers. In addition, a radar pulse is known to penetrate into a dry snowpack, with backscatter being a combination of surface scatter originating from the snow surface and volume scatter from density variations and ice layers within the snowpack, the melt-affected surface from the previous summer (hereafter, the 'last summer surface'), and potentially deeper (Scott et al., 2006; Rignot et al., 2001). Comparison of elevations derived from radar altimetry and laser altimetry (for which penetration is negligible) suggest that slope corrections are the major source of uncertainty, but that a metre-scale bias resulting from penetration of the pulse into the snowpack and firn can occur (Schröder et al., 2017; Michel et al., 2014).

Numerous studies have revealed rapid changes of glaciers, ice caps, and the margins of the Greenland and Antarctic ice sheets (Smith et al., 2020; Wouters et al., 2019), areas characterised by sloping terrain and hence uncertainty in measurements obtained from traditional satellite radar altimeters. In 2010 the European Space Agency (ESA) launched CryoSat-2, a radar altimetry satellite designed for cryospheric monitoring, specifically to overcome the limitations of previous generations of radar altimeters (Wingham et al., 2006; Drinkwater et al., 2004). CryoSat-2 carries the Synthetic Aperture Interferometric Radar Altimeter (SIRAL), which is operated in Low resolution mode (LRM) over the interior of the ice sheets, Synthetic Aperture Radar mode (SAR) over sea ice, and Interferometric Synthetic Aperture Radar mode (SARIn) over glaciers, ice caps, and the margins of the ice sheets. In SARIn mode the Doppler shift of the returned signal is used to divide the footprint into ~300 m along-track strips, and dual receiving antennas used to locate the scatterer in the across-track direction, allowing three-dimensional location of ground echoes. Retracker algorithms for land ice applications have tended to focus on the leading edge of the SARIn mode waveforms, identifying the point the leading edge exceeds a threshold (Helm et al., 2014; Wouters et al., 2015), or locating the steepest slope of the leading edge (Gray et al., 2013; Nilsson et al., 2016), though others use the entire waveform (Bouzinac, 2012). In addition to POCA elevations, where the across-track slope lies within a suitable range (~0.5° to ~2.0°) it is also possible to obtain a swath of additional geolocated elevation estimates (Gray et al., 2013; Gourmelen et al., 2018). CryoSat-2 SARIn-mode therefore has the advantages of a considerable increase in the density of elevation estimates and the three-dimensional geolocation of the POCA and swath points with *a priori* knowledge of subsatellite topography only used as a reference to pick the most likely solution (see Section 3.1).

Assuming it is possible to accurately geolocate elevation estimates, this leaves the penetration of the radar pulse into the snowpack as the major source of uncertainty in elevations derived from CryoSat-2. Under dry snowpack conditions, the backscatter returned to SIRAL is a combination of returns from the snowpack surface, and volume scattering from density variations and ice layers within the snowpack, as well as the last summer surface, and potentially from the underlying firn and ice (Gray et al., 2019; Arthern et al., 2001). SIRAL lacks the resolution to distinguish between returns from the surface and subsurface (Hawley et al., 2013; Gray et al., 2019). The strength of the return from the last summer surface is often the strongest (Gray et al., 2019), with the potential to lead to a 'penetration bias' between the elevation estimated from the altimetry and the physical surface of the glacier.

Considerable data collection (ESA CryoSat Validation Exercise, CryoVEx (Skourup et al., 2012, 2012, 2018; Hvidegaard et al., 2015)) and research (Sandberg Sørensen et al., 2018; Gray et al., 2017) has been devoted to CryoSat-2 calibration and validation. Gray et al. (2017) compared POCA and swath points with reference elevations from Devon ice cap in the Canadian Arctic and the western Greenland margin, finding a minimum bias for a satellite roll angle correction of ~0.0075°. The accuracy of the satellite roll angle arrays (and therefore derived elevations, particularly in the swath) has since been improved in the BaselineD data by correcting the mispointing angles calculated from onboard star trackers for the aberration of light (Scagliola et al., 2018). A remaining metre-scale bias is attributed to the penetration of the signal into the snowpack (Gourmelen et al., 2018, 2017; McMillan et al., 2013). Sandberg Sørensen et al. (2018) presented a comparison and validation of CryoSat-2 POCA points derived from six different retrackers with respect to airborne laser scanner data over western Austfonna collected in April 2016. Retrackers which focus on the leading edge of the waveform were found to produce the best agreement with the laser transect elevations. These retrackers exhibited a negative bias over smooth surface areas, as would be expected from the penetration of the radar signal into the dry snowpack. Whereas over surging areas with crevasses, a positive bias was observed. This is attributed to the coarser footprint of CryoSat-2, where the leading edge of the waveform will arise from high points such as serac tops, whereas the 100 × 100 m averaged laser data will measure both the tops of seracs and into deep crevasses, resulting in a lower average surface. Other studies have compared rates of elevation change derived from CryoSat-2 and repeat airborne laser overflights, with small differences likely due to different data collection intervals (McMillan et al., 2018; Wouters et al., 2015; Gourmelen et al., 2018).

This study uses data from snowmobile-based Global Navigation Satellite System (GNSS) transects and laser altimeter overflights of the Austfonna ice cap, Svalbard, to measure the bias between the glacier surface (defined as the snowpack surface when and where snow is present, otherwise the ice surface) and elevations derived from CryoSat-2 SARIn-mode radar altimetry, as well as the effect of this bias on mass balance estimation. It provides a thorough assessment of a leading-edge retracker and swath processor (Gray et al., 2013, 2015, 2017, 2019), which has many similarities to other processing schemes for deriving POCA (Helm et al., 2014; Nilsson et al., 2016) and swath (Gourmelen et al., 2018; Foresta et al., 2016, 2018; Smith et al., 2017) elevations of glaciers and ice sheets. Measurements of surface elevation from snowmobile-mounted GNSS transects and laser altimeter overflights are used as a calibration dataset to assess the elevation biases of both POCA and swath points derived from CryoSat-2 SARIn-mode data, as well as the variability in these biases at the transition from volume scattering to surface scattering dominance at the onset of surface melt. Quantifying these biases may aid in their attribution and inform strategies to mitigate them in future processing of radar altimetry data. Next, the effect of the temporal variability in bias on time series of cumulative elevation/mass change is discussed, as well as the potential to extract additional information on snowpack thickness. Surface elevation change rates derived from repeat GNSS/airborne laser transects are used as a validation dataset for estimates of ice cap-wide elevation change rates calculated using a least-squares plane-fit algorithm and hypsometric polynomial applied to CryoSat-2 POCA and swath points at 1 km^2 resolution.

2. Study area

Here, the bias between CryoSat-2 radar altimetry POCA and swath elevation estimates and the glacier surface, and its potential effect on mass balance estimation is investigated using an extensive calibration/validation dataset from the Austfonna ice cap (Fig. 1). Austfonna - located between 21°E and 27°E, and 79.25°N and 80.25°N - is situated on the island of Nordaustland in the Norwegian Arctic archipelago of

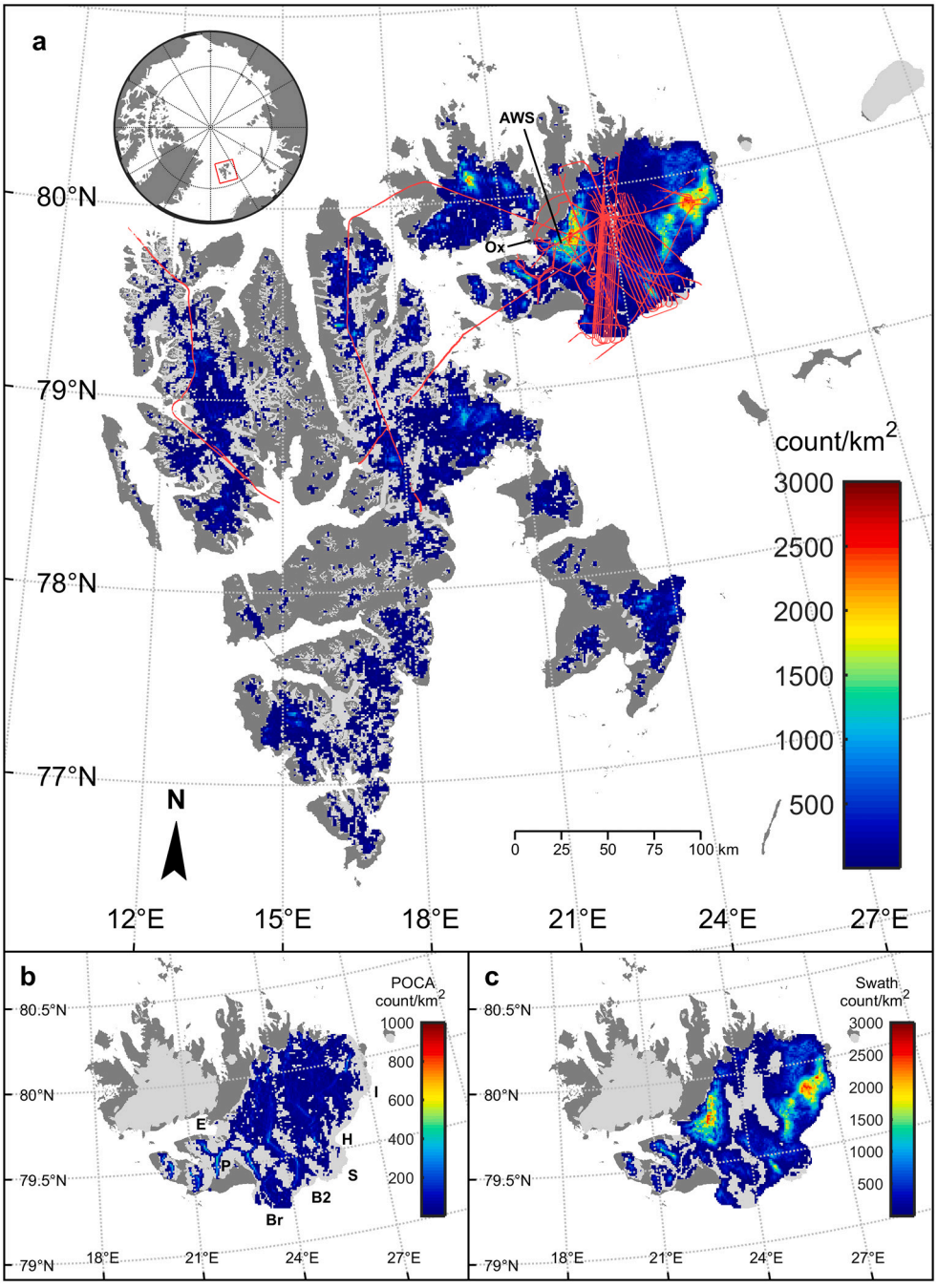

Fig. 1. Map of the study area and data coverage. (a) Count of combined CryoSat-2 SARIn POCA and swath points over glacier surfaces in Svalbard (2011–2017), gridded at 1 km resolution. Glacier areas not covered by POCA or swath points are shown in light gray (ice-free terrain in dark gray). Red lines show snowmobile-mounted GNSS and airborne laser transects across the ice cap. Black lines point to the Eton-2 Automatic Weather Station (AWS) and Oxfordhalvøya depot (Ox). Inset: location of the Svalbard archipelago within the Arctic. (b) POCA and (c) Swath coverage of Austfonna (note the different scale bars). Letters in b refer to glaciers mentioned in the text (E: Etonbreen, P: Palanderisen, Br: Bråsvellbreen, B2: Basin-2, S: Storisstraumen, H: Hartogbukta, I: Italiabreen). (For interpretation of the references to color in this figure legend, the reader is referred to the web version of this article.)

Svalbard. At ~8000 km^2 Austfonna is one of the largest ice caps in the Eurasian Arctic. Bamber et al. (2004) observed thickening of the Austfonna interior using data from airborne laser overflights in 1996 and 2002. Raper et al. (2005) and Bamber et al. (2004) suggested that this widespread thickening was likely a response to increased snowfall as a result of sea ice decline in the Barents Sea. However, an analysis of equilibrium line mass fluxes (Bevan et al., 2007) demonstrated that 75% of the mass gain in the accumulation zone occurred in three surge-type basins in their quiescent phases (Etonbreen (E in Fig. 1b), Bråsvellbreen (Br), and Storisstraumen/Basin-3 (S), the latter of which has since surged (Dunse et al., 2015)), suggesting dynamic imbalance as the main reason for thickening. A geodetic mass-balance assessment showed a net thickening between 2003 and 2008 (Moholdt et al., 2010), but retreat of the calving cliffs of the southern margin resulted in an overall negative mass balance (Moholdt et al., 2010; Dowdeswell et al., 2008). Mass loss from the ice cap has increased in recent years, mainly as a result of the onset of the surge of Storisstraumen and neighbouring glaciers after 2012 (Dunse et al., 2015; McMillan et al., 2014), and the speed up of a few other glaciers on the southern and eastern margins (Strozzi et al., 2017), contributing significantly to the overall mass loss from Svalbard glaciers (Schuler et al., 2020; Morris et al., 2020; Tepes et al., 2021). Due to the rapid geometric changes of surging glaciers, the Storisstraumen basin is excluded from the estimation of elevation bias following the onset of the surge in 2012 (Dunse et al., 2015).

3. Data

The Norwegian Polar Institute (NPI) and University of Oslo (UiO) have conducted annual mass balance and altimetry-calibration field campaigns on Austfonna since 2004. GNSS data have been collected

along consistent mass balance transects and varying transects designed to provide calibration data for ESA-coordinated airborne campaigns, CryoSat-2, and ICESat-1/2. Snowpack thickness is sounded approximately every 2 km along each transect, to aid in the processing of ground penetrating radar data. Snow depth, ice melt, and ice flow is measured at mass balance stakes, and snow density and stratigraphy are analysed at a number of pits spread across the ice cap. Meteorological observations are collected at Automatic Weather Stations on both sides of the main divide (Schuler et al., 2014), whilst snow accumulation is measured by ultrasonic distance rangers. In addition, the Technical University of Denmark (DTU; 2011, 2012, 2014 and 2016), the Alfred Wegner Institute and NASA Operation IceBridge (OIB; 2017) have conducted airborne radar and laser scanning flights over Austfonna, with some flights replicating ground transects. The availability of surface elevation transects from GNSS and airborne laser scanning, and snowpack thickness/last summer surface depth, provide an extensive dataset for estimation of CryoSat-2 elevation biases, and validation of $\frac{dh}{dt}$ derived from the application of a least-squares plane-fitting technique to a time-series of CryoSat-2 SARIn POCA and swath elevation estimates (Morris et al., 2020).

In addition to the datasets detailed, a 20 m resolution digital elevation model (DEM) [NPI, 2014, supplementary figure 1] was used in the extrapolation of CryoSat-2-derived $\frac{dh}{dt}$ to unsurveyed areas and to correct for surface slopes in elevation bias estimation. Randolph Glacier Inventory 6.0 (RGI6.0) shapefiles [Pfeffer et al., 2014; Consortium, 2017; Nuth et al., 2013, supplementary figure 2] were used to define the extent of the ice cap and the surging basins.

3.1. CryoSat-2

This study utilises all available CryoSat-2 L1b BaselineC data covering Austfonna during the period 1st January 2011 to 31st December 2017. Erroneous roll angle arrays were updated using the star tracker mispointing angle corrections (Scagliola et al., 2018). The maximum slope retracker and swath processor of Gray et al. (2013, 2015, 2017, 2019) was used to derive geolocated POCA and swath elevation estimates. Waveform power coupled with the sine and cosine of the phase is used to create complex waveforms from the data in the L1b files. For each ~300 m along-track, a low-pass-filter is applied to the real and imaginary components of the complex waveform such that when recombined into power and phase, the geocoding is improved and the height noise reduced due to the lower phase noise. The delay time to the POCA is assumed to be represented by the maximum slope on the first significant leading edge of the power waveform, with corresponding values of phase and coherence. POCAs with a coherence below 0.7 are discarded. The three-dimensional location of the POCA (latitude, longitude, height above the WGS84 ellipsoid) is calculated from the delay time, satellite positioning and altitude, and across-track angle calculated from the phase difference between the two antennas. At delay times greater than the POCA, the waveform contains backscatter from either side of the POCA, as well as subsurface returns. In the presence of an across-track slope in the range ~0.5° to ~2.0° an across-track swath of additional geolocated elevation estimates can be obtained. It is assumed that as the POCA is displaced upslope, the area downslope is more strongly illuminated by the main beam and hence dominates the differential phase returns over the range-ambiguous area upslope [e.g. Gray et al., 2013, figure 1]. The phase difference is unwrapped in both directions starting from the central region of high coherence, and used along with satellite positioning, interferometric baseline, and delay time to derive swath elevations. Estimation of latitude, longitude and elevation is performed three times by adding and subtracting 2π to the phase values. The selection of the most likely solution (-2π, 0, $+2\pi$) is based on the difference between the elevation estimates and the elevations obtained by interpolating a reference DEM to the corresponding location. For each swath segment the mean, standard deviation and elevation difference at the start and end of the segment are calculated. The choice is then based on the minimum of the sum of these values for the three options. Finally, the swath points are averaged in ~100 m across-track segments. The orbital inclination of CryoSat-2 and the topography of Austfonna are particularly conducive to swath processing in the western basins north of the main divide, and the eastern basins south of the main divide, as evidenced by the high point density shown in Fig. 1a and c centred around 23°E, 79.75°N and 26°E, 79.75°N. High POCA densities are primarily found on the drainage divides of the smaller connected ice cap Palanderisen (P), on the western side of Austfonna, centred on 22°E, 79.5°N (Fig. 1b).

Echoes from ice covered surfaces were isolated using the Svalbard Glacier inventory (Nuth et al., 2013; Consortium, 2017). Additional points were discarded if the internal tracking loop 'lost lock' entirely (Aublanc et al., 2018) or if the receiving window was incorrectly positioned to detect the initial backscatter from within the footprint (and hence part of the rising limb of the waveform was missed) by removing any waveform with an initial backscatter value greater than two times the standard deviation from the mean of the initial values of the other waveforms from that satellite pass.

3.2. Global navigation satellite system

GNSS transects were collected as part of annual mass balance and satellite altimetry calibration field campaigns (Table 1). A GNSS base station (Topcon Legacy E+ receiver in 2011-2016, Leica GS10 receiver in 2017) was installed at the Oxford peninsula depot ('Ox' in Fig. 1a), and operated continuously throughout the field campaigns. 'Rover' GNSS receivers were mounted to two snowmobiles, and operated whenever the snowmobiles left the depot. One snowmobile towed a sledge carrying a Topcon Legacy E+ receiver and antenna, and a ground penetrating radar. The second snowmobile carried a Trimble NetR9, NetR8, or NetR5, and a pole-mounted antenna. Antenna height above the snow surface was repeatedly measured, accounting for compaction of the upper layers of the snowpack by the snowmobile. Antenna height above the snow surface was subtracted from the GNSS heights so the elevation transects were representative of the snow surface.

The base station antenna was mounted on a hut at the depot. The position of the depot is kept as a fixed point in ETRS89 coordinates, and measured to a reference point at Carfaxhaugen (<2 km) and to the

Table 1
Timing of Global Navigation Satellite System (GNSS) and Airborne Laser Scanner (ALS) elevation transect collection (NPI: Norwegian Polar Institute. UiO: University of Oslo. DTU: Technical University of Denmark. OIB: NASA Operation IceBridge).

Year	Data	Institution	Date (DD/MM/YY)
2011	GNSS	NPI/UiO	01/05/2011–08/05/2011
	ALS	DTU (Skourup et al., 2012)	30/04/2011
2012	GNSS	NPI/UiO	30/04/2012–04/05/2012
	ALS	DTU (Skourup et al., 2012)	28/04/2012
2013	GNSS	NPI/UiO	01/05/2013–07/05/2013
	ALS	-	-
2014	GNSS	NPI/UiO	01/05/2014–06/05/2014
	ALS	DTU (Hvidegaard et al., 2015)	03/05/2014
2015	GNSS	NPI/UiO	01/05/2015–05/05/2015
	ALS	-	-
2016	GNSS	NPI/UiO	14/04/2016–24/04/2016
	ALS	DTU (Skourup et al., 2018)	15/04/2016–16/04/2016
2017	GNSS	NPI/UiO	28/04/2017–08/05/2017
	ALS	OIB	06/04/2017

International GNSS Service/Norwegian Mapping Authority station in Ny-Ålesund. Data were processed using Topcon Positioning Systems Pinnacle 1.0 software. The positions of the rovers were estimated at 1 second intervals based on a double difference solution of L1 and L2c frequencies from both Global Positioning System (GPS) and GLONASS signals. Signals from satellites less than 15° above the horizon are discarded. The dual frequencies allow correction for ionospheric conditions, and the Goad Goodman troposphere model (Goad and Goodman, 1974) is used to correct for lower atmospheric conditions.

As a consistency check, the kinematic GNSS data were also post-processed with precise point positioning (PPP) using the online application of the Canadian Spatial Reference System (CSRC) with final GNSS satellite orbit ephemerides and clock corrections from the International GNSS Service (IGS). This produces absolute coordinates for the rover antenna that are independent of the base station. The differential and absolute processing chains are consistent within 5-10 cm both horizontally and vertically. Comparison of repeat-track GNSS surface elevations from different survey days in the same field campaign results in an average annual standard deviation of 10–15 cm for either processing technique, which includes both measurement uncertainties and short-term (<2 weeks) surface elevation changes due to factors such as snowfall, snowdrift and snowmobile-track compression.

3.3. Airborne laser scanner

Airborne laser scanner data (Table 1) were collected and processed by the Technical University of Denmark (DTU) as part of CryoSat Validation Experiment (CryoVEx) campaigns (2011, 2012, 2014 and 2016 (Skourup et al., 2012, 2012, 2018; Hvidegaard et al., 2015)), and by NASA's Operation IceBridge (2017 (Studinger et al., 2010)). CryoVEx campaigns collected airborne laser altimetry (Riegl LMS Q-240i) and radar altimetry (Airborne SAR/Interferometric Radar System (ASIRAS), an airborne precursor of SIRAL) data, as well as GPS and Inertial Navigation System (INS) data for aircraft positioning and attitude measurement over land ice in Greenland, Svalbard, and the Canadian Arctic, and over sea ice in the Arctic Ocean. The laser scanner surveys a swath of ~300 m around aircraft nadir to a vertical accuracy of ~10 cm. The standard deviation of crossover elevations was found to be between 5 cm and 10 cm (Skourup et al., 2012, 2012, 2018; Hvidegaard et al., 2015).

Operation IceBridge was initiated to fill the gap in spaceborne laser altimetry observations between the end of the ICESat mission in February 2010 and the launch of ICESat-2 in September 2018 (Studinger et al., 2010). The primary focus is on the ice sheets, with annual surveying of the Antarctic ice sheet, and annual or seasonal surveying of the Greenland ice sheet. The ice caps of the Canadian Arctic archipelago have been surveyed in occasional years, and a number of transects around Svalbard were flown in Spring 2017. These flights utilised the Airborne Topographic Mapper (ATM), a scanning LIDAR with an accuracy better than 10 cm, as well as GPS and INS for measuring aircraft positioning and attitude.

Six CryoVEx transects across Austfonna were flown in 2011, two approximating CryoSat-2 tracks, four aligned with ground transects (Skourup et al., 2012). Six transects were flown in 2012, three approximating CryoSat-2 tracks and three ASIRAS validation lines (Skourup et al., 2012). Two parallel lines approximating a CryoSat-2 track (accounting for off-nadir POCAs) were flown in 2014, along with ASIRAS validation lines (Hvidegaard et al., 2015). A dense grid of parallel transects aligned with CryoSat-2 tracks along Bråsvellbreen (Br) and Storisstraumen (S) were flown in 2016 (Skourup et al., 2018; Sandberg Sørensen et al., 2018). In 2017 Operation IceBridge flew two transects across Austfonna, replicating the 1996 and 2002 transects of Bamber et al. (2004). Some data gaps exist at high elevation due to the presence of clouds.

CryoVEx data were supplied by S. Simonsen at DTU, Operation IceBridge data were downloaded from the data portal (nsidc.org/icebridge/portal/map). CryoVEx data from 2011, 2012 and 2014 were supplied with a point separation of ~7 m, CryoVEx data from 2016 and Operation IceBridge data from 2017 were supplied with a point separation of ~1.5 m. All datasets were utilised at the supplied resolution.

As a cross-validation between surface GNSS and airborne laser glacier surface elevation measurements, the two datasets were compared in overlapping areas for each annual campaign, with a maximum time separation of 4 weeks. All annual biases between the two datasets were within 15 cm, and the average annual standard deviation was 13 cm. These numbers can be considered as the approximate accuracy and precision for the validation of CryoSat-2 elevations and related elevation biases.

3.4. Snow probing

Snow depth was sounded using avalanche probes (~3 m-long pointed metal poles marked every 1 cm, designed to locate persons buried by avalanches) approximately every 2 km along the GNSS transects conducted as part of the annual field campaigns on Austfonna. At each location, the estimated snow depth is the average of at least three soundings spaced a few metres apart, discarding obvious outliers defined by high variability in probed depth over a short horizontal distance. Complications arise where impenetrable ice layers within the snowpack result in an underestimation of snowpack thickness, or the penetration of the probe into underlying firn results in an overestimation. The depth of any hard layers (which could represent ice layers within the seasonal snowpack or the snow-firn interface) are also noted, and used in combination with closely located snow pits and adjacent (~2 km distance) soundings along a transect to give a best estimate of snowpack thickness (and hence 'last summer surface' depth). Probed snow depths are converted to an estimate of ice cap average snow depth by fitting a first order polynomial to probed depths and elevations from a digital elevation model, then applying this on a 1 km^2 grid, accounting for the glacier fraction within each grid cell.

3.5. Automatic weather station

An automatic weather station (AWS) installed at an elevation of ~400 m on the northwestern flank of Austfonna ('AWS' in Fig. 1a) has been operated since spring 2004 (Schuler et al., 2014, 2007). This is located near the second lowest mass balance stake of the Etonbreen transect, and is hereafter referred to as 'Eton-2 AWS'. The AWS measures air temperature, humidity, wind speed and direction, and radiation components (Schuler et al., 2014). Additional instruments include a thermistor string and an ultrasonic distance ranger. Here, positive temperatures are taken as a proxy for ice-cap-wide surface melting (especially when temperatures are particularly high or persistently positive), and ultrasonic distance ranger data are used to reveal the varying snowpack and ice surface height.

4. Methods

4.1. Elevation bias in dry snow

The extensive GNSS and airborne laser transects across Austfonna reliably measure the elevation of the snowpack surface, providing a dataset with which to assess the bias between the glacier surface and quasi-coincident CryoSat-2 POCA and swath elevation estimates. The elevations of CryoSat-2 points and GNSS or airborne laser points with a small spatiotemporal offset are compared. The distance offset is limited to 500 m, ensuring a large number of pairs are found. The temporal offset is limited to 30 days prior to or following the date of collection of GNSS or airborne laser transects, this again ensures that a sufficient number of pairs are found, although does allow for the potential for limited snowpack surface elevation change through accumulation, redistribution, compaction or melt.

Given the large distance offset limit, it is necessary to correct for the surface elevation difference between the location of the CryoSat-2 point and the location of the GNSS/airborne laser point. The 20 m DEM is used for this correction. For each point pair a subsection of the DEM is extracted that is 1 pixel in each direction greater than the maximum north–south and east–west area covered by the two points. The elevation gradients in the east and north direction for this section of DEM are calculated. Using the gradients in east and north directions and the distance between the CryoSat-2 point and GNSS/airborne laser point, a correction is applied to remove the influence of the sloping terrain on the elevation bias. This has a negligible impact on the mean/median elevation bias estimate, but decreases the standard deviation (histograms exhibit a sharper peak, but the location of the peak is unchanged). Pairs with an elevation difference larger than ±10 m were rejected, along with pairs from the surging basin Storisstraumen from 2012 onwards as the elevation differences were dominated by rapid surface elevation changes and crevassing (Sandberg Sørensen et al., 2018) due to the surge (Dunse et al., 2015) rather than signal penetration into the snowpack.

4.2. Seasonality of elevation bias

The GNSS and airborne laser elevation transects collected annually in late-April and early-May (Table 1) can also be used as a 'reference surface', representative of '(near) end of accumulation season' snowpack elevation, with which to assess the changing elevation bias through time. Here, it is used to assess the elevation bias over seven months (January to July). This comprises a first period of five months (January to May) when the snowpack is typically cold and dry, the elevation of the physical surface is increasing due to snowfall, and backscatter is dominated by volume scattering, and a second period of two months (June and July) when surface melting becomes widespread, the glacier surface lowers as first snow then ice melts, and a transition from volume scattering to surface scattering dominance occurs.

The same procedure as outlined in Section 4.1 is used to find pairs of CryoSat-2 and GNSS/airborne laser points, and to correct for the slopes between the locations of the points. CryoSat-2 points are grouped by calendar month and compared to all April/May GNSS and airborne laser transects from the appropriate year. The results from each month are then combined with the corresponding months from other years, to give an average seasonality in elevation bias for the study period.

In practice, the timing of onset of melt varies between different years, and begins at low elevation and propagates to higher elevations. In addition, short-lived melt and rain events can occur even in winter (Østby et al., 2017). This means that some months, likely particularly June, will comprise a combination of bias estimates from both melting and non-melting areas of the snowpack. However, combining corresponding months from different years will reveal general patterns of bias seasonality.

4.3. Elevation change and mass balance

Repeat GNSS and airborne laser transects can also be used as a validation dataset for elevation (and hence mass) change estimates derived from CryoSat-2 data. This section describes the processing of CryoSat-2 data from POCA and swath elevation estimates to maps of elevation change rate and a time series of mass change using 'residuals'.

CryoSat-2 POCA and swath points were grouped into 1 km^2 grid cells. Several different resolutions were tested, and 1 km^2 was found to provide the best compromise between retaining small-scale detail in $\frac{dh}{dt}$ mapping, providing sufficient areal coverage to minimise the need to extrapolate to unsurveyed regions, whilst also ensuring most grid cells contain a large number of elevation estimates and limiting the topographic complexity within each grid cell.

For each grid cell, an iterative least squares regression method with outlier (±10 m) removal is used to simultaneously fit a plane characterising the slopes in the east and north directions, and to calculate the linear rate of elevation change (Moholdt et al., 2010; Morris et al., 2020):

$$f(x, y, t) = c_1 x + c_2 y + \frac{dh}{dt} t + v \quad (1)$$

where x, y and t are easting, northing and time offsets between each point and the mean, c_1 and c_2 are the surface slope gradients in the east and north directions, $\frac{dh}{dt}$ is the linear rate of elevation change, and v are the elevation residuals in the regression. Grid cells containing fewer than 10 elevation estimates, fewer than 4 individual satellite passes, or a span of less than 2 years between first and last elevation estimate (in practice, most are greater than 6 years (supplementary figure 3)), are rejected (Wouters et al., 2015). Offsets between each individual elevation estimate and the modelled plane and linear rate of elevation change ('residuals') are also calculated. These are later spatially extrapolated and used to add seasonality and interannual variations to the linear rate of volume and mass change.

The generally simple topography of an ice cap such as Austfonna leads to extensive spatial coverage of CryoSat-2 elevation estimates (Fig. 1). For mass balance estimation, a third-order hypsometric polynomial was used to extrapolate to unsurveyed areas (Morris et al., 2020). CryoSat-2 has a 30 day orbital subcycle, suggesting the possibility to resolve volume changes at monthly resolution (Ciracì et al., 2018; Noël et al., 2018). Following filtering, there are >15 CryoSat-2 passes over Austfonna each month, spread across the longitudinal range of the ice cap. For each month, the average monthly residual was calculated if the grid cell contained an elevation estimate, and extrapolated to the remainder of the ice cap using a first-order relationship between residual and elevation (Morris et al., 2020).

The linear rate of volume change can be calculated from the sum of the elevation change rates of the grid cells multiplied by the ice area within each grid cell. A time-series of cumulative volume change, including seasonal and interannual variability, can be derived by adding monthly residual volumes to the linear rate of volume change.

A density assumption is required to convert linear rates and time-series of cumulative volume change to mass change estimates. The appropriate density assumption can deviate significantly from the density of ice for short-term geodetic surveys (Huss, 2013). For an observation period >5 years, where the mass balance gradient is stable, firn present, and volume changes are large, Huss (2013) recommends a density assumption of 850 ± 60 kgm^{-3}. This value is adopted here for the conversion of volume change to mass change estimates. This overestimates the seasonal mass cycle (as the snowpack density is lower than the density of ice), but is appropriate for conversion of long-term rates. Further details on processing and mass balance results for Svalbard can be found in Morris et al. (2020).

4.4. Validation

A number of the GNSS transects were repeated annually to a precision of 10 m, whilst coordination between the field teams with those conducting overflights means some laser altimetry transects correspond to GNSS transects. In addition, there are a large number of crossover points between GNSS and/or airborne laser transects. This repeated collection of surface elevation data at a consistent time towards the end of the accumulation season (late-April/early-May) minimises the impact of seasonal elevation changes and means it is possible to construct a spatially extensive $\frac{dh}{dt}$ dataset which can be used as a 'validation dataset' for the $\frac{dh}{dt}$ estimates from CryoSat-2, assuming steady rates of elevation change during the CryoSat-2 period.

To assemble this dataset, a method similar to that of McMillan et al. (2018) was used. The rate of elevation change between GNSS/airborne laser point pairs with a horizontal separation of <10 m was calculated.

Point pairs within Storisstraumen but prior to the onset of the surge in 2012 (Dunse et al., 2015) are rejected, as rates of elevation change increased greatly after 2012. No correction is applied for the slope between the point pair, as it is assumed that the correction would be negligible over <10 m, and that the dataset is sufficiently large that positive and negative corrections would cancel each other out. The rate of elevation change for a 1 km^2 grid cell is calculated as the average of all the point pair elevation change rates within it. This can then be compared to the corresponding grid cell in the CryoSat-2-derived elevation change rate map.

4.5. Snow depth

The known transition from volume scattering when a snowpack is cold to surface-dominated scattering when a snowpack is wet suggests the possibility to measure snowpack thickness if the last summer surface is a sufficiently strong reflector to dominate the volume scattering. Here, four methods are tested to estimate bulk snowpack thickness from extrapolated CryoSat-2 residuals, informed by the elevation bias assessment detailed in Sections 4.1 and 4.2, and compared with estimates from snow probing: (1) POCA and swath point residuals are grouped by calendar month and extrapolated using a first order relationship between residual and elevation, as for mass balance estimation. The estimated end-of-winter snowpack depth is the apparent elevation

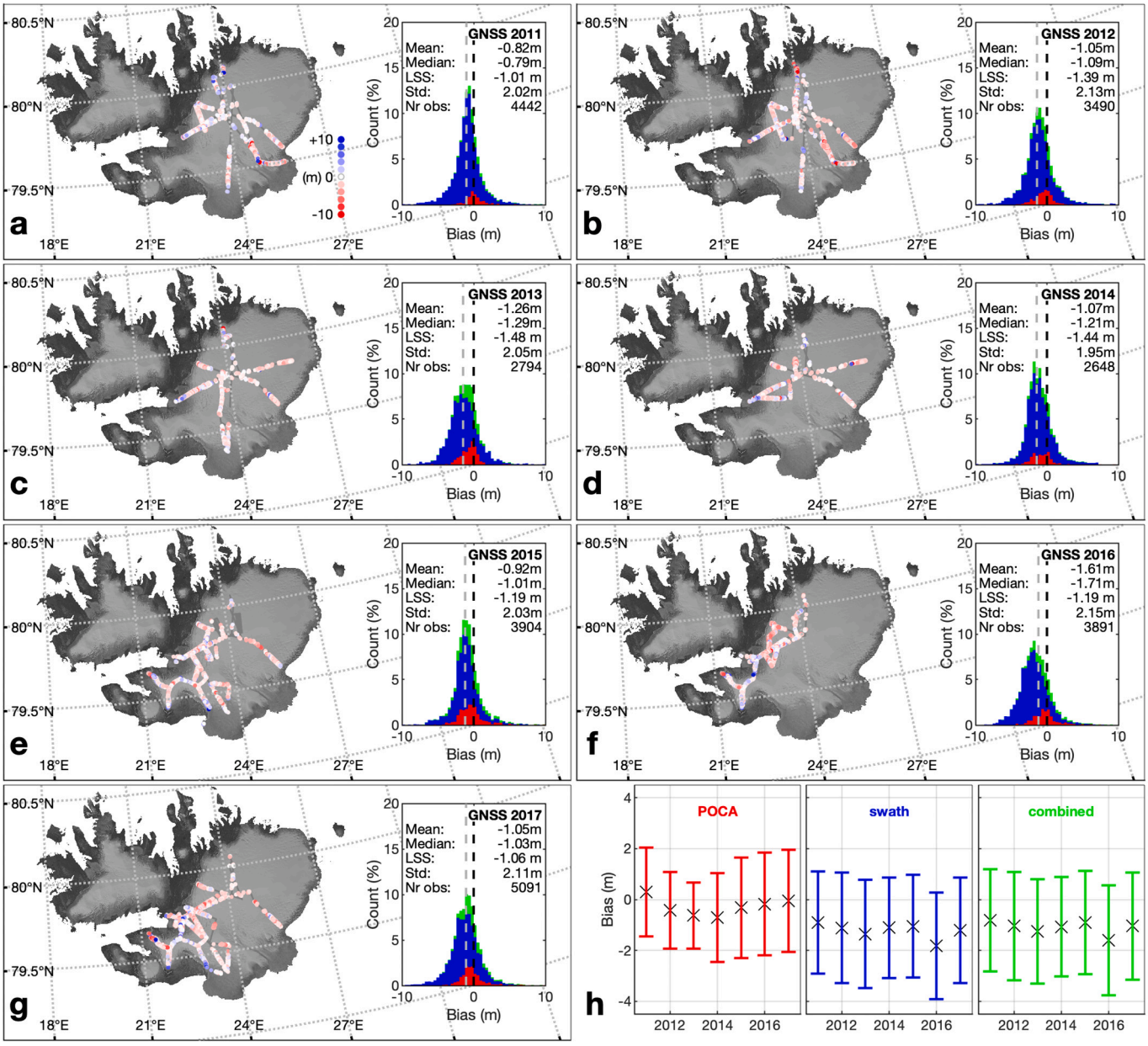

Fig. 2. Annual elevation bias in dry snow along GNSS transects collected in late-April and early-May. (a–g) Maps of elevation bias (POCA/swath elevation minus GNSS elevation) for the years 2011–2017. Insets: Histograms of elevation bias in 0.4 m bins between -10 m and +10 m for POCA (red), swath (blue), and combined (green). Dashed lines show the snow surface (black) and reconstructed last summer surface (LSS; gray). Values are given for combined points mean and median elevation bias, standard deviation (Std), LSS depth, and the number of observations (Nr obs). (h) Graphs of yearly mean bias and standard deviation for POCA (red), swath (blue), and combined (green) elevations. Background Landsat-8 OLI image courtesy of the U.S. Geological Survey. (For interpretation of the references to color in this figure legend, the reader is referred to the web version of this article.)

increase between winter and summer. This is the simplest method, and ignores both the exact timing of melt onset, and the progressive delay at higher elevations. (2) The same method using solely swath point residuals. (3) Grouping and extrapolating swath point residuals using a 30-day moving window and assuming the largest increase observed in any realisation is representative of snowpack thickness. This allows the onset of melt to occur at any time, but does not account for altitudinal variability. (4) As 3, but recording the increase in individual grid cells, thus allowing for altitudinal variability.

5. Results

Annual maps and histograms of the elevation bias of CryoSat-2 POCA and swath points with respect to the GNSS and airborne laser transects for the years 2011 to 2017 are shown in Figs. 2 and 3. The peak of the elevation bias histograms is generally on the negative side of the 0 m line (black dashed line), demonstrating that on average the radar elevation is below the physical surface of the glacier. It is apparent that the bias differs between POCA (red histograms) and swath points (blue histograms). The swath histograms consistently peak around 1–1.5 m below the glacier surface. The same is true for the combined histograms (green), as a result of the dominance of swath points. The peak of these histograms often approximately coincides with the depth of the annual last summer surface (gray dashed line) inferred from snow probing observations. The histograms of POCA points peak closer to the 0 m line, but often have a distribution skewed towards penetration. In order to address the limited number of POCA observations, additional GNSS surveys were conducted in 2015–2017 (Fig. 2e–g) on the Palanderisen ice cap ('Y' shaped transects centred on 22°E, 79.5°N, P in Fig. 1b). The prominent drainage divides on this ice cap are the point of closest approach for a number of satellite passes, and hence a high number of POCA points lie within 500 m of transects driven along the divides. The annual mean elevation bias and standard deviation of POCA (red), swath (blue), and combined points (green) shown in Figs. 2h and 3f shows POCA points generally close to the surface and swath points 1–1.5 m below, a pattern that is consistent year-on-year, and between the independent GNSS and airborne laser datasets. Increasing (decreasing) the distance limit increases (decreases) the number of observations but does not significantly change the results.

The GNSS and airborne laser transects are collected in late spring (Table 1), prior to the onset of widespread surface melt. Therefore, the elevation biases observed in Figs. 2 and 3 are representative of dry snowpack conditions, and therefore backscatter with a dominant contribution from the subsurface. They are likely typical for many Arctic glaciers and ice caps at the end of winter. Comparable transects are not available for the melt season, so the spring transects are used as a proxy or 'reference surface' for '(near) end of accumulation season' glacier surface elevation. Combining all years gives a sufficient number of point pairs to construct monthly histograms of POCA (red), swath (blue) and combined points (green) bias with respect to the reference surface (Fig. 4). The histogram of POCA points consistently peaks close to the surface, with a decreased skew towards penetration in June and July. The elevation bias of swath points shifts from 1–1.5 m between January and May to a distribution centred close to the surface in June and July. It should be noted that as the melt season progresses the representativeness of the reference surface decreases as snow and ice melt reduces

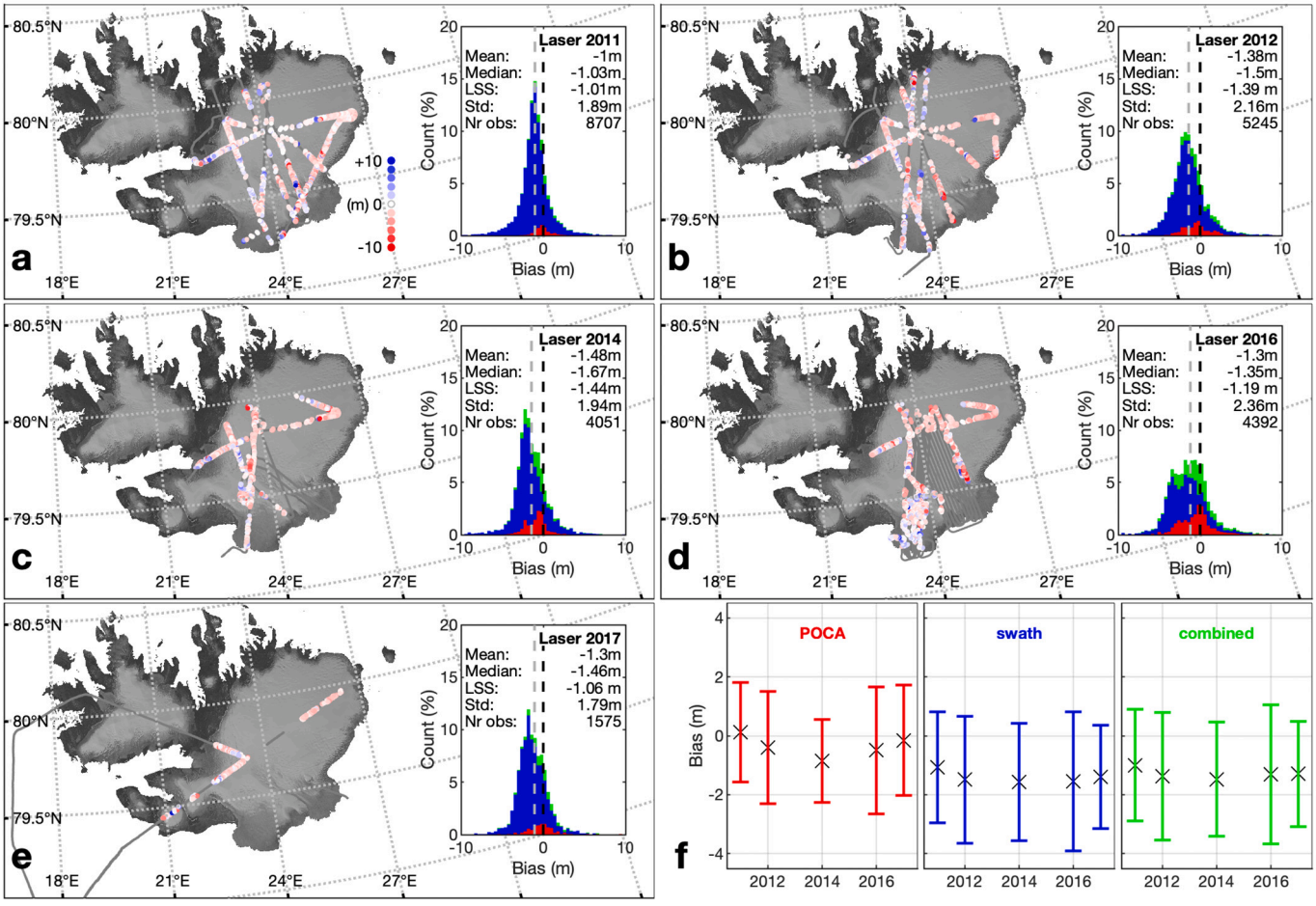

Fig. 3. Annual elevation bias in dry snow along airborne laser transects collected in late-April and early-May. As Fig. 2 for airborne laser transects in 2011, 2012, 2014, 2016, and 2017. (For interpretation of the references to color in this figure legend, the reader is referred to the web version of this article.)

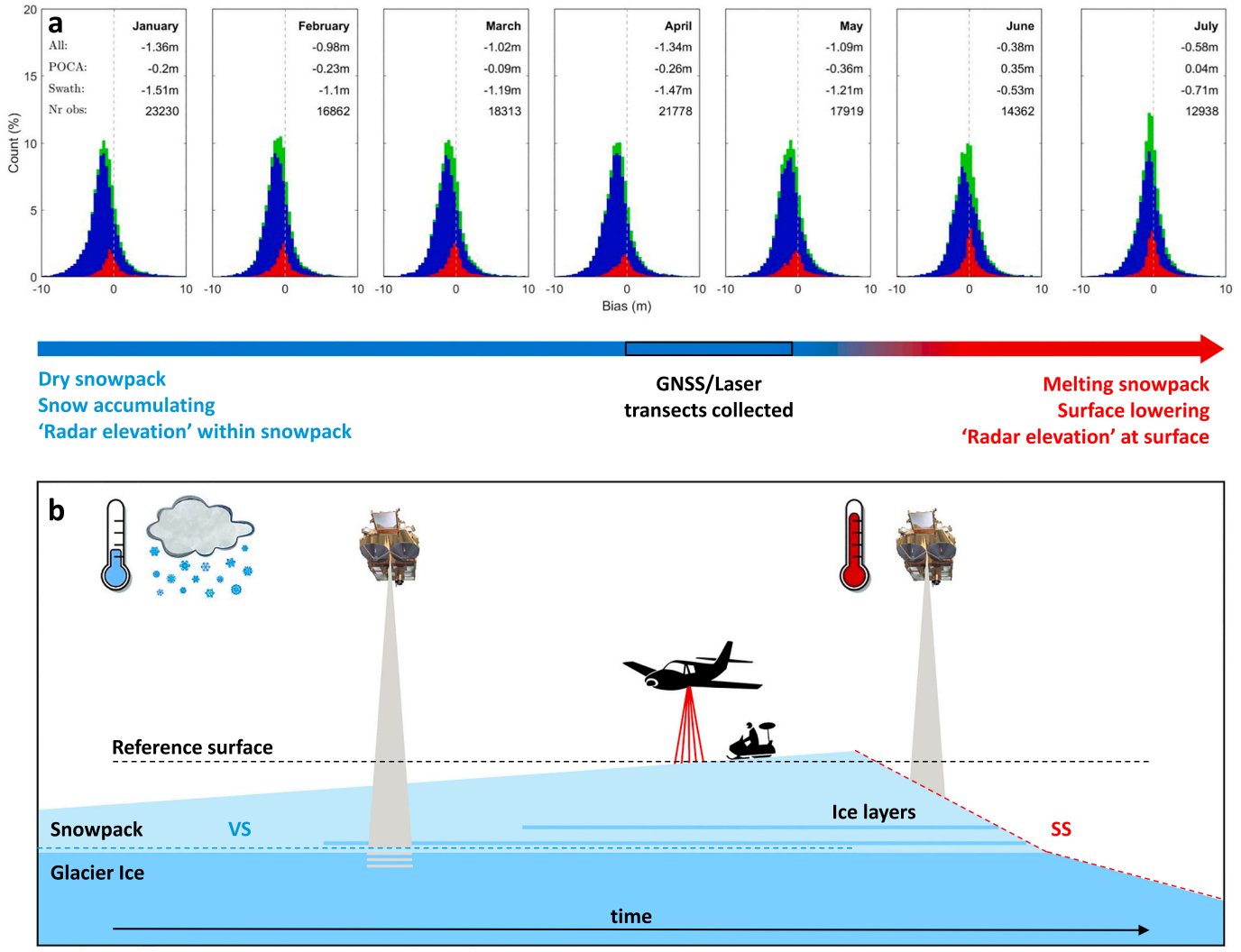

Fig. 4. Seasonal elevation bias along GNSS and airborne laser transects. (a) Histograms of elevation bias for POCA (red), swath (blue), and combined (green) for winter months (January–May) and summer months (June–July) relative to the reference surface of the GNSS and airborne laser transects collected from late-April to early-May each year. Values are given for combined, POCA, and swath mean biases and number of observations (Nr obs). (b) Schematic of snow/ice surface elevation and 'radar elevation' through the accumulation and ablation seasons and accompanying transition from volume scattering (VS) to surface scattering (SS), relative to the reference surface of the GNSS and airborne laser transects. The dashed line shows the approximate dominant radar reflection horizon, at the surface during melt and near the snow-ice interface otherwise. CryoSat-2 data were collected continuously, GNSS and airborne laser transects were collected in late-April and early-May. Schematic is representative of the ablation area of the ice cap, some snow will survive the summer at higher elevations. (For interpretation of the references to color in this figure legend, the reader is referred to the web version of this article.)

surface elevation.

This change in the radar reflection horizon is evident in time series of elevation and mass change (Fig. 5). The apparent ice cap mass is approximately constant throughout the winter, increases rapidly at the beginning of summer, before falling rapidly later in the summer. This is particularly evident in the non-surging (gray) and combined (blue) time-series, likely due to the smaller impact of the shift in bias in the rapidly thinning surging basin (red). Consistent with Fig. 4, these 'jumps' in elevation/mass are found to coincide with the onset of persistent surface melt at the Eton-2 AWS (Fig. 5a). The time series of surface elevation from the ultrasonic distance ranger on the Eton-2 AWS (Fig. 5b) shows the actual pattern of seasonal elevation, and hence mass change, with a gradual increase each winter as snow accumulates, and a rapid fall each summer when the temperature rises above 0°C.

Though the seasonal change in radar reflection horizon impacts seasonal mass balance estimation, the lack of an interannual trend in the elevation bias (Figs. 2h and 3f) means the effect on long term estimates of mass balance is minimal. Estimates of elevation change along closely repeating (<10 m) GNSS and airborne laser scanner transects are consistent in magnitude and spatial pattern with ice-cap-wide estimates from CryoSat-2 (Fig. 6a). The gradual thickening of the quiescent surge-type basins Etonbreen (E) and Bråsvellbreen (Br), as well as in the high accumulation areas in the southeast upstream of Italiabreen (I) is evident in both datasets. Moderate thinning is observed in the lower reaches of Etonbreen and Bråsvellbreen, and in Hartogbukta (H). Rapid thinning is observed in both datasets in the surging Storisstraumen (S) and the neighbouring surging glacier, Basin-2 (B2). Comparing corresponding GNSS/airborne laser scanner and CryoSat-2 elevation change grid cells (Fig. 6b and c) leads to good agreement, with most surge (red) and non-surge (black) points lying close to the identity line, though some considerable outliers exist. These points originate from the ice divide between Storisstraumen and Etonbreen, and the interior of the smaller surging basin (Fig. 6d).

The validation dataset clearly demonstrates that the application of a least-squares plane-fit algorithm to CryoSat-2 elevation measurements is capable of accurately resolving the long-term elevation change signal.

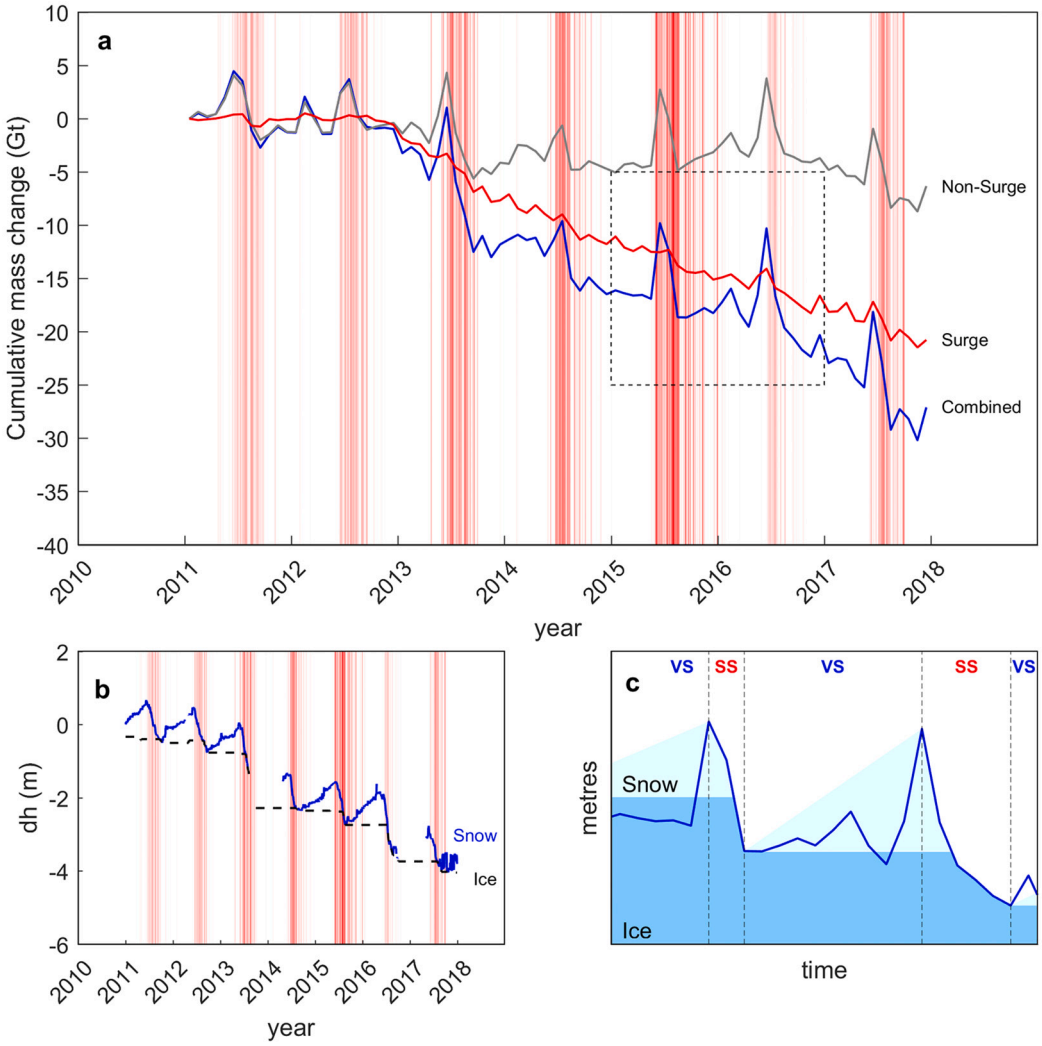

Fig. 5. Interpretation of cumulative mass change time series. (a) Cumulative mass changes of Austfonna, 2011–2017, for non-surging ice (gray), surging ice (red), and the entire ice cap (blue), calculated by applying a least-squares plane-fit algorithm to CryoSat-2 points and utilising the residuals. Red lines (a and b) correspond to days with positive temperatures (a proxy for surface melt) recorded at the Eton-2 AWS, with intensity denoting relative temperature (solid red denotes 10°C, decreasing intensity denotes lower temperatures down to 0°C. The high temperatures in summer 2014 and 2015 are likely due to sensor drift, which would explain the unexceptional annual mass loss compared to the extreme 2013 melt season (Lang et al., 2015). The sensor was replaced in Spring 2016). Positive spikes in the cumulative mass change time series can be seen to coincide with the onset of prolonged and persistent positive temperatures. The dashed box denotes the extent of panel c. (b) Time series of snowpack surface (solid blue) from an ultrasonic distance ranger, and ice surface (dashed black) from annual mass balance stake measurements at the Eton-2 AWS. The wintertime snowpack accumulation is not seen in the CryoSat-2 time series in panel a, whereas melt season surface lowering is evident in both datasets. The gaps in the ultrasonic distance ranger time series between summer 2013 and spring 2014, and between late summer 2016 and spring 2017 were caused by the melt out of the stake on which the instrument was mounted. (c) Schematic demonstrating the effect of the transition from volume scattering (VS) to surface scattering (SS) at the onset of melt on the cumulative mass change time series. During the winter, the altimeter tracks a relatively consistent surface near the base of the snowpack, underestimating mass gain. A 'jump' occurs at the onset of melt, as the altimeter tracks the snowpack surface. (For interpretation of the references to color in this figure legend, the reader is referred to the web version of this article.)

However, Fig. 5 shows that the seasonal mass cycle is incorrectly characterised as a result of the changing of the dominant radar reflection horizon at the onset of melt and its effect on the penetration bias primarily of the swath points (Figs. 2, 3 and 4). The close correspondence between swath penetration depth and last summer surface depth in winter, and the raising of the radar reflection horizon to the surface at the onset of melt suggest the possibility to remotely estimate bulk snowpack thickness in the absence of ground-based GNSS or airborne/spaceborne laser altimeter data, which would allow for more accurate characterisation of the seasonal mass cycle. Various methods were tested, and compared with values extrapolated from snow probing data (Fig. 7). In all cases the estimates were within the spread of probed values, and occasionally close to the bulk value estimated from the probed values and their altitudinal spread, but no method was able to consistently replicate the estimate from probing or the pattern of interannual variability.

6. Discussion

6.1. Elevation bias

Comparison of CryoSat-2 elevation estimates with snowmobile-mounted GNSS and airborne laser transects (Figs. 2 and 3) reveals an elevation bias due to the penetration of the radar signal into the dry snowpack. There is also a difference between the elevation biases of POCA and swath elevation estimates. Whilst the retracker performs well and POCA points tend to be a good approximation for the glacier surface, on average swath points tend to exhibit a penetration bias of

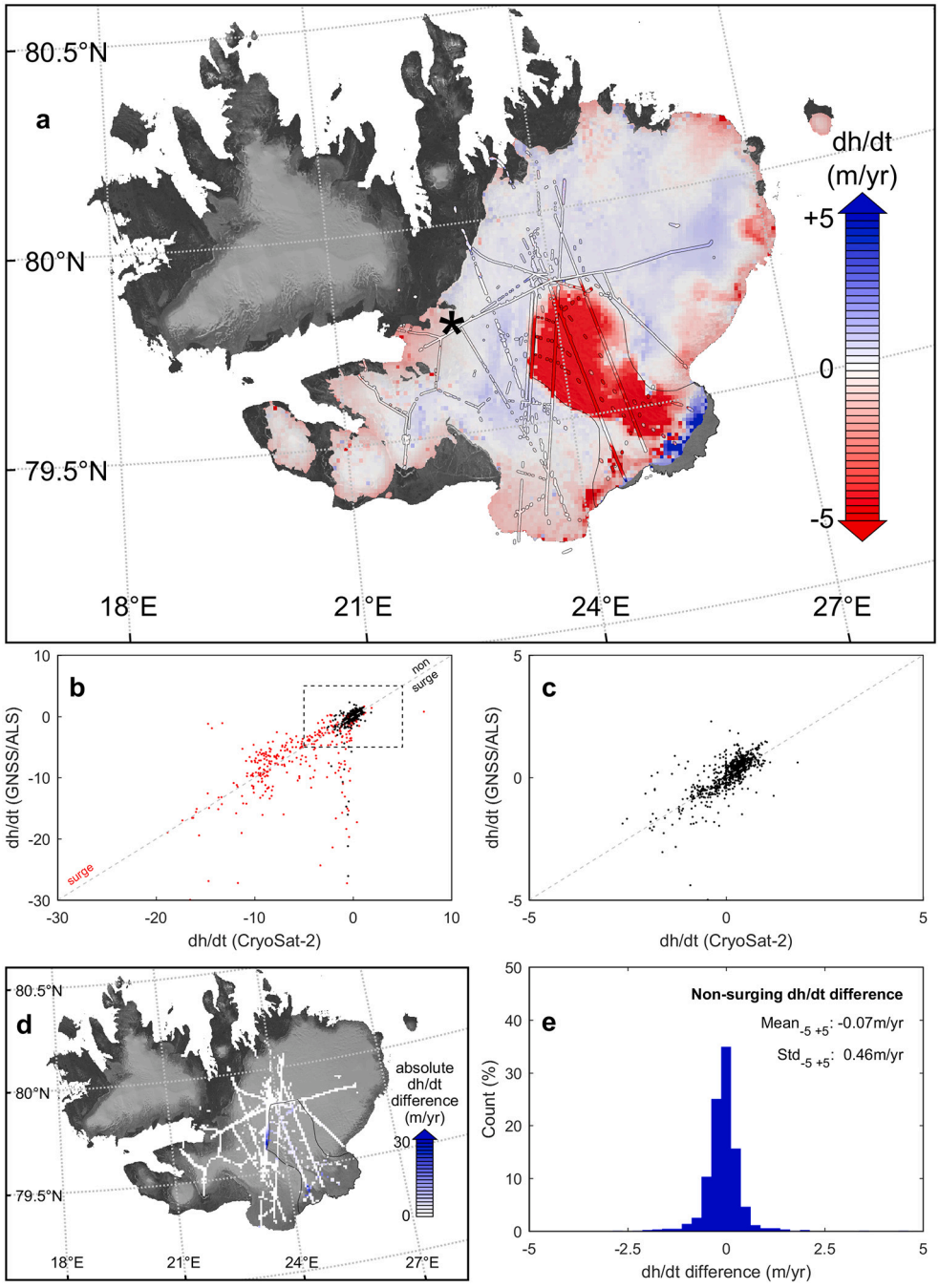

Fig. 6. Validation of Austfonna CryoSat-2 $\frac{dh}{dt}$ using GNSS/Airborne laser 'validation dataset'. (a) $\frac{dh}{dt}$ along repeat transects and CryoSat-2 $\frac{dh}{dt}$ from combined POCA and swath points. Asterisk (*) shows the location of the AWS. (b) Scatter plot of CryoSat-2 $\frac{dh}{dt}$ against validation $\frac{dh}{dt}$ for surging (red) and non-surging (black) ice, showing a small number of points deviate significantly from the identity line. The dashed box denotes the extent of panel c (c) Scatter plot of non-surging ice. (d) Absolute $\frac{dh}{dt}$ difference showing the location of large deviations (blue) at the margins of the surge. (e) Histogram of $\frac{dh}{dt}$ difference of non-surging ice. Background Landsat-8 OLI image (a and d) courtesy of the U.S. Geological Survey. (For interpretation of the references to color in this figure legend, the reader is referred to the web version of this article.)

1–1.5 m. Swath elevation estimates are much more numerous than POCA elevation estimates (Fig. 1b and c), and therefore the mean elevation bias of all elevation estimates combined (POCA and swath) is approximately the same as the mean elevation bias of the swath points alone. However, this will vary spatially, both on the scale of the ice cap, and a wider study area such as the entire archipelago of Svalbard as the ability to retrieve swath points is dependent on satellite orbital inclination and subsatellite topography (Fig. 1). Gourmelen et al. (2018) similarly found a 1–2 m penetration bias for swath elevations compared to OIB laser elevations at three sites in Greenland and Antarctica. Their corresponding POCA penetration bias was in all cases smaller than the swath bias, but larger than the bias observed here.

The differing bias between POCA and swath elevation estimates is not surprising given the different methodology used in extracting geolocated elevation estimates from the waveform; the POCA resulting from the use of a retracker, unlike the swath points. The retracker is able to resolve the initial increase in backscatter from the snowpack surface, whilst the swath points are located at the dominant radar reflection horizon (the larger POCA penetration bias in Gourmelen et al. (2018) likely results from differing retracker design). However, it is encouraging to note that the standard deviation of swath points is not considerably greater than that of POCA points (Figs. 2h and 3f), both around 2 m with respect to the GNSS and airborne laser data. In addition to penetration, it is not possible to rule out geolocation errors arising from phase errors due to range ambiguous returns from the opposite side of the POCA, imperfect roll correction, phase noise or imperfect receiver phase calibration as a source of bias between the CryoSat-2 elevations and the surface transects (Gray et al., 2013; Sandberg Sørensen et al., 2018), though this is mitigated by the large number of comparisons.

The mean penetration bias of swath points approximates the last

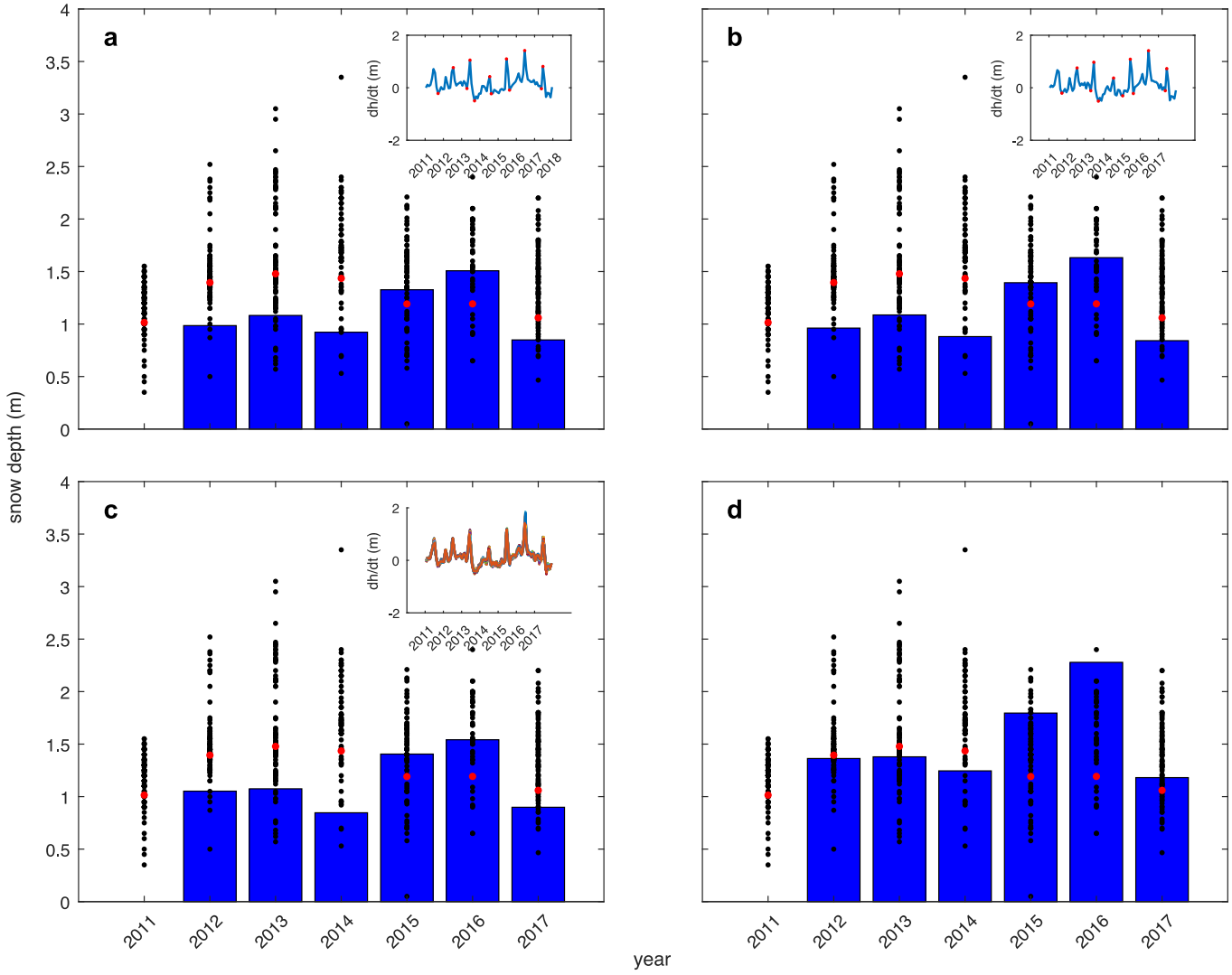

Fig. 7. Estimated end-of-winter snowpack thickness, 2012–2017 (blue bars) from annual minima and maxima elevation residuals for non-surging basins of Austfonna, compared to estimated area-averaged snow depth (red) from snow probing (black). (a) Using all elevation measurements (POCA and swath) and divided by calendar month. Inset: detrended time-series of elevation change (blue) and annual minima and maxima (red). (b) Using only swath elevation measurements and divided by calendar month. Inset: detrended time-series of elevation change (blue) and annual minima and maxima (red). (c) Using all elevation measurements, dividing into 30 day segments for extrapolation, and iteratively shifting the division by 1 day, to find the largest jumps. Inset: 30 realisations of detrended elevation time-series. (d) Grid cell-by-grid cell maximum jump analysis. (For interpretation of the references to color in this figure legend, the reader is referred to the web version of this article.)

summer surface, likely the dominant radar reflection horizon as a result of the density difference between a cold and dry winter snowpack and underlying glacier ice, superimposed ice or firn surface from the end of the previous melt season, along with potential ice layers close to the snowpack base resulting from short-lived late season melt events or rain-on-snow events, as have been observed in snowpits on Austfonna. Further study should be devoted to establishing whether the close correspondence between swath penetration bias and last summer surface depth observed here is replicated in thicker snowpacks (for example, Icelandic ice caps, Alaskan or Patagonian icefields) or whether the greater thickness and likely presence of ice layers from short-lasting melt or rain events in these more maritime snowpacks results in a radar elevation within the snowpack. Data from the tandem operation of CryoSat-2 and ICESat-2 could make this possible, demonstrating whether the elevation bias is regionally variable and consistent with snow depths measured in the field, potentially allowing routine monitoring of snow depth and better characterisation of the seasonal mass cycle from space.

The elevation bias of swath points is greatly reduced in the summer months (Fig. 4a), as the onset of persistent surface melt (Fig. 5a) leads to a transition from volume- to surface-dominated backscatter. Whilst the ultrasonic distance ranger data demonstrates that snow accumulates gradually and persistently throughout the winter (Fig. 5b), the altimetry shows apparent stability of the surface elevation and mass throughout the winter (Fig. 5a). This is because the last summer surface is the dominant radar reflection horizon, whilst the overlying snowpack is comparatively invisible to the altimeter, meaning the altimeter consistently tracks the last summer surface through the winter (Fig. 4a, January to May). The result is an underestimation of the seasonal mass gain through snowfall through winter. The seasonal mass increase is only observed at the onset of melt, as water forms at the surface of the snowpack, masking out deeper returns and resulting in a 'jump' in elevation observed by Cryosat-2 (Fig. 4a, June and July; The positive POCA elevation bias in June may reflect additional snow accumulation between the collection of GNSS/airborne laser transects and the onset of melt). Though the apparent elevation increase seems to be indicative of

the total winter snow accumulation, the seasonal mass signal is overestimated in the time series due to the use of a volume-to-mass conversion factor close to the density of ice, a value that is appropriate for converting the long-term trend (Huss, 2013). Fig. 5c shows a schematic of this process in terms of glacier surface elevation and radar reflection horizon through two winter (VS - volume scattering) and summer (SS - surface scattering) seasons (and Fig. 4b shows this with reference to the timing of data collection).

6.2. Elevation change and mass balance validation

There is a strong correspondence between the CryoSat-2 and validation $\frac{dh}{dt}$ datasets on both broad and small spatial scales (Fig. 6a). Both capture a general pattern of interior stability or gradual thickening, with thickening most pronounced south of the main divide, particularly in the southeast of the ice cap (upstream of Italiabreen (I), around 26°E, 79.8°N). Whilst GNSS coverage is sparse near the ice cap margins due to the difficulty and risk involved in operating snowmobiles in crevassed areas, they do concur with CryoSat-2 estimates of gradual thinning where transects do reach low elevations (for example, Etonbreen (E), Hartogbukta (H), and Bråsvellbreen (Br)). On a smaller scale, both the CryoSat-2 and validation datasets resolve the spatially variable rates of elevation change in the surging basins (Storisstraumen (S) and the neighbouring Basin-2 (B2) to the west). Two continuous transects cover the length of Storisstraumen. From north to south, the eastern transect shows rapid thinning in the north of the basin, a region of lower magnitude thinning/near stability halfway between the summit and margin, then a further region of rapid thinning, and finally at the south of the transect a region of negligible change where the transect crosses on to stable ice at the divide between Storisstraumen and Basin-2. The western transect crosses from the rapidly thinning ice of Storisstraumen, to the stable ice of the divide, and to the smaller surging basin (Basin-2). In this small basin, both the Cryosat-2 and validation datasets resolve rapid interior thinning and thickening close to the margin.

Plotted against one another (Fig. 6b and c) points from the CryoSat-2 and validation datasets generally lie close to the identity line. Non-surging ice points form a cluster around 0, as ice thickening or thinning is generally gradual (Fig. 6c). Elevation change of surging ice is more rapid, and though many points lie close to the identity line, there is a greater spread, and some considerable mismatches (Fig. 6b). These are located at the ice divide between Storisstraumen and Etonbreen, and the interior of Basin-2 (Fig. 6d). They result from the changing rate of elevation change as more ice is mobilised into the surge, and the surge of Storisstraumen 'pirates' ice from the neighbouring Etonbreen basin. The CryoSat-2 results provide a single estimate of the average $\frac{dh}{dt}$ for each grid cell (generally using data with a time span of over six years (supplementary figure 3)), whereas the GNSS and airborne laser transects provide a snapshot of $\frac{dh}{dt}$ with a time interval of between one and six years. The shorter the time interval of the GNSS and airborne laser points the greater the potential for a mismatch with the corresponding CryoSat-2 grid cell, where $\frac{dh}{dt}$ was temporally variable. No clear inverse relationship between interval and $\frac{dh}{dt}$ difference is apparent for non-surging ice, likely due to gradual and relatively steady $\frac{dh}{dt}$, whereas the spread of mismatch values increases with decreasing GNSS/airborne laser time interval within the surging basins, as expected from the time evolving rate of elevation change. Removing all $\frac{dh}{dt}$ comparisons within the surging basin and outliers ($<$-5 myr^{-1} and $>$5 myr^{-1}) to account for the ice at the divide between Etonbreen and Storisstraumen, it is possible to calculate statistics for the difference between the CryoSat-2 $\frac{dh}{dt}$ and validation $\frac{dh}{dt}$ (Fig. 6e). The histogram peaks at a difference of -0.125 myr^{-1} to +0.125 myr^{-1} (mean of -0.07 myr^{-1}) with ~90% of points between -0.625 myr^{-1} and +0.625 myr^{-1}. The difference is close to zero, with a standard deviation of 0.46 myr^{-1} (rising to 1.56 myr^{-1} if the points at the divide between Etonbreen and Storisstraumen are not removed).

Gourmelen et al. (2018) found a difference of 0.04 myr^{-1} between swath $\frac{dh}{dt}$ and OIB laser-scanner-derived $\frac{dh}{dt}$ for Amundsen Sea sector and Jakobshavn area, compared to 0.40 myr^{-1} and 0.17 myr^{-1} respectively for POCA versus OIB $\frac{dh}{dt}$. The greater accuracy of $\frac{dh}{dt}$ estimates using swath appears primarily a result of the one to two orders of magnitude increase in the number elevation measurements, affording a higher spatial resolution of $\frac{dh}{dt}$ mapping (Gourmelen et al., 2018, figure 10) rather than a preference for swath elevation estimates over POCA elevation estimates. Fig. 1b and c shows that both are necessary to achieve maximum spatial coverage of an ice cap such as Austfonna, whilst the increase in elevation estimates provided by swath processing is much lower in the more rugged terrain characteristic of Spitsbergen (the main island of the Svalbard archipelago (Morris et al., 2020)), or mountainous regions.

In all, the validation dataset shows that, in spite of the seasonal changes in the radar reflection horizon shown in Figs. 2, 3 and 4, applying a least-squares plane-fitting technique to multi-year swath processed CryoSat-2 SARIn mode data produces robust estimates of elevation change for non-surging ice. For surging ice, validation is complicated by temporal variability in the rate of elevation change, and whilst frequent airborne laser transects would be capable of resolving time variable rates of elevation change that may be useful for studying surge dynamics, CryoSat-2 provides spatially extensive and temporally integrated estimates of elevation change suitable for mass balance assessment.

6.3. Snow depth

Despite the general correspondence between swath penetration bias and the last summer surface inferred from snow probing, it did not prove to be possible to replicate the magnitude and interannual variability of bulk snowpack thickness from CryoSat-2 data alone. This is likely due to the use of first order polynomial relationships between residuals/probed snow depths and elevation to extrapolate the sparse measurements, which would not resolve the differences in snowpack thickness north and south of the main ice divide (Taurisano et al., 2007). Other factors such as backscatter from ice layers within the snowpack resulting from short-lived wintertime melt events or rain-on-snow events, or conversely from deeper layers within the firn pack could introduce spatially varying differences between the CryoSat-2 elevation and the last summer surface. It is also difficult to conclude whether simpler or more complex methods perform best, as all are limited by the extrapolation. The three simpler methods (Fig. 7a, b, c) are closer to the probing based estimate for 2015 and 2016, which are greatly overestimated by the more complex method (Fig. 7d). However, the more complex method performs well in 2012, 2013 and 2014, while overestimating 2015 and 2016. It is therefore only possible to conclude that whilst the estimates of swath penetration bias presented here (Figs. 2 and 3) suggest the potential to measure seasonal snowpack thickness from space, further study is necessary to realise and validate this goal.

7. Conclusions

GNSS and airborne laser transects from the Austfonna ice cap, Svalbard were used to assess the elevation bias of POCA and swath elevations derived from CryoSat-2 BaselineC SARIn-mode data, and the $\frac{dh}{dt}$ results from the application of a least-squares plane-fit algorithm. Erroneous roll angle arrays were replaced using the star tracker mispointing angle corrections, meaning the results presented also apply to the recently released BaselineD dataset. Under cold snowpack conditions POCA points were found to be located close to the snowpack surface, though with a distribution skewed towards penetration. Swath points exhibit a greater elevation bias of 1 to 1.5 m below the snow surface. This is interpreted as resulting from the penetration of the radar signal into a dry snowpack with the strongest reflection from the last

summer surface, which is to some degree overcome for the POCA points by the leading-edge retracker employed. The swath point penetration bias therefore approximates the snowpack thickness on Austfonna, and further investigation in areas of different snowpack conditions should be conducted to assess whether swath points reliably resolve this interface, with a view to assessing seasonal snow depth from space. The elevation bias is reduced at the onset of surface melt when signal penetration reduces and both POCA and swath points are located close to the snowpack surface. However, melt season surface elevation transects would be useful in confirming this result, due to the potential for surface elevation change between the collection of GNSS/airborne laser transects in late-April and early-May and the onset of surface melting 1–2 months later.

In spite of the seasonally varying elevation bias of POCA and swath points, the application of a least-squares plane-fit algorithm to multi-year CryoSat-2 SARIn-mode POCA and swath points was found to provide robust estimates of elevation change rates. $\frac{dh}{dt}$ along repeat (<10 m) GNSS and airborne laser transects were compared with the CryoSat-2 results, showing excellent agreement in both surging and non-surging basins. Mismatches were found at the margins of the surge of Storisstraumen and inland of the surge of Basin-2, which were attributable to inland propagation of the surges captured at different times in the two $\frac{dh}{dt}$ datasets. Whilst a least-squares plane-fit algorithm provides robust estimates of multi-year elevation change, consideration should be given to the differing biases of POCA and swath points and the seasonality of swath point bias when CryoSat-2 elevations are used to construct or geolocate digital elevation models for change detection, or for short-term (~annual) $\frac{dh}{dt}$ surveys. In the latter case the bias seasonality caused by the changing radar reflection horizon has the potential to lead to spurious $\frac{dh}{dt}$ estimates, and favours the use of data from the end of the melt season and prior to significant wintertime snow accumulation (Gray et al., 2019).

The correspondence between the penetration bias of swath points and the last summer surface motivated investigation of whether snowpack thickness could be sensed remotely from CryoSat-2 alone. However, none of the methods tested accurately reproduced independent estimates from snow probing in the field. It is likely that more complex extrapolation methods are necessary to reproduce the spatial variability in snowpack thickness observed on Austfonna. Further research on the penetration bias in deeper and melt/rain affected snowpacks is necessary to establish whether the correspondence between penetration depth and the last summer surface is particular to snowpacks analogous to Austfonna, or more widely the case for other glacier regions in different climate regimes.

Credit author statement

AM performed data processing and led the writing of the manuscript. GM designed the study and assisted in data processing. LG wrote the CryoSat-2 retracker and swath processor. TVS processed data from the automatic weather station/ultrasonic distance ranger. TE processed the GNSS data. AM, GM, TVS and TE have participated in NP/UiO fieldwork on Austfonna. All authors contributed to the writing and revision of the manuscript.

Declaration of Competing Interest

The authors declare that they have no known competing financial interests or personal relationships that could have appeared to influence the work reported in this paper.

Acknowledgments

This research was funded by the Research Council of Norway programme for Space Research (ROMFORSKNING), project number 251355/F50. Norwegian Polar Institute/University of Oslo field campaigns on Austfonna, including CryoSat-2 calibration and validation activities have been partly funded by European Space Agency PRODEX and CryoVEx programmes. CryoSat-2 L1b and STR mispointing angles data were provided by the European Space Agency (ESA). Further information on the custom software used to process the CryoSat-2 data to geocoded height data can be obtained from L.G. Airborne laser data were provided by the Technical University of Denmark through ESA CryoVEx/CryoVal-LI projects (2011,2012,2014,2016) and NASA's Operation IceBridge (2017). GNSS observations, snow depth probing and AWS data were collected during joint annual field campaigns by the Norwegian Polar Institute and University of Oslo, with major funding contributions from the CryoVEx and PRODEX programs (Contracts 4000110724/25) of the European Space Agency and various research projects funded by the Research Council of Norway, in particular the program for Space Research (ROMFORSKNING) project 251355/F50. The Svalbard Integrated Observing System (SIOS) is acknowledged for support to research infrastructure at Austfonna. Thanks to everyone who has contributed to data collection, processing and fieldwork through the years. The Geodetic Survey of Canada is acknowledged for the free CSRS-PPP service for GNSS processing (https://webapp.geod.nrcan.gc.ca/geod/tools-outils/ppp.php). Glacier outlines and high resolution DEMs of Svalbard can be obtained from the Norwegian Polar Institute Dataset catalogue https://data.npolar.no/dataset. Landsat-8 OLI data available from the U.S. Geological Survey (https://earthexplorer.usgs.gov). The anonymous reviewers are thanked for their constructive comments which significantly improved the manuscript.

Appendix A. Supplementary data

Supplementary data to this article can be found online at https://doi.org/10.1016/j.rse.2021.112805.

References

Arthern, R.J., Wingham, D.J., Ridout, A.L., 2001. Controls on ERS altimeter measurements over ice sheets: footprint-scale topography, backscatter fluctuations, and the dependence of microwave penetration depth on satellite orientation. J. Geophys. Res. Atmos. 106 (D24), 33471–33484. https://doi.org/10.1029/2001JD000498.

Aublanc, J., Moreau, T., Thibaut, P., Boy, F., Rémy, F., Picot, N., 2018. Evaluation of SAR altimetry over the Antarctic ice sheet from CryoSat-2 acquisitions. Adv. Space Res. 62 (6), 1307–1323. https://doi.org/10.1016/j.asr.2018.06.043.

Bamber, J., Krabill, W., Raper, V., Dowdeswell, J., 2004. Anomalous recent growth of part of a large Arctic ice cap: Austfonna, Svalbard. Geophys. Res. Lett. 31 (12) https://doi.org/10.1029/2004GL019667.

Bevan, S., Luckman, A., Murray, T., Sykes, H., Kohler, J., 2007. Positive mass balance during the late 20th century on Austfonna, Svalbard, revealed using satellite radar interferometry. Ann. Glaciol. 46, 117–122. https://doi.org/10.3189/172756407782871477.

Bouzinac, C., 2012. CryoSat Product Handbook. European Space Agency.

Brenner, A.C., Blndschadler, R.A., Thomas, R.H., Zwally, H.J., 1983. Slope-induced errors in radar altimetry over continental ice sheets. J. Geophys. Res. Oceans 88 (C3), 1617–1623. https://doi.org/10.1029/JC088iC03p01617.

Ciracì, E., Velicogna, I., Sutterley, T.C., 2018. Mass balance of Novaya Zemlya archipelago, Russian high arctic, using time-variable gravity from GRACE and altimetry data from ICESat and Cryosat-2. Remote Sens. 10 (11), 1817. https://doi.org/10.3390/rs10111817.

Consortium, R.G.I., 2017. Randolph Glacier Inventory - a dataset of global glacier outlines: version 6.0, Tech. rep. Global Land Ice Measurements from Space, Colorado, USA.

Dowdeswell, J.A., Benham, T.J., Strozzi, T., Hagen, J.O., 2008. Iceberg calving flux and mass balance of the Austfonna ice cap on Nordaustlandet, Svalbard. J. Geophys. Res. Earth Surf. 113 (F3) https://doi.org/10.1029/2007JF000905.

Drinkwater, M.R., Francis, R., Ratier, G., Wingham, D.J., 2004. The European Space Agency's Earth Explorer mission CryoSat: measuring variability in the cryosphere. Ann. Glaciol. 39, 313–320. https://doi.org/10.3189/172756404781814663.

Dunse, T., Schellenberger, T., Hagen, J.O., Kääb, A., Schuler, T.V., Reijmer, C.H., 2015. Glacier-surge mechanisms promoted by a hydro-thermodynamic feedback to summer melt. Cryosphere 9 (1), 197–215. https://doi.org/10.5194/tc-9-197-2015.

Foresta, L., Gourmelen, N., Pálsson, F., Nienow, P., Björnsson, H., Shepherd, A., 2016. Surface elevation change and mass balance of Icelandic ice caps derived from swath mode CryoSat-2 altimetry. Geophys. Res. Lett. 43 (23), 12138–12145. https://doi.org/10.1002/2016GL071485.

Foresta, L., Gourmelen, N., Weissgerber, F., Nienow, P., Williams, J.J., Shepherd, A., Drinkwater, M.R., Plummer, S., 2018. Heterogeneous and rapid ice loss over the Patagonian ice fields revealed by CryoSat-2 swath radar altimetry. Remote Sens. Environ. 211, 441–455. https://doi.org/10.1016/j.rse.2018.03.041.

Goad, C.C., Goodman, L., 1974. A modified hopfield tropospheric refraction correction model. In: Paper Presented at the Fall Annual Meeting American Geophysical Union, p. 1974.

Gourmelen, N., Goldberg, D.N., Snow, K., Henley, S.F., Bingham, R.G., Kimura, S., Hogg, A.E., Shepherd, A., Mouginot, J., Lenaerts, J.T.M., Ligtenberg, S.R.M., van de Berg, W.J., 2017. Channelized melting drives thinning under a rapidly melting Antarctic ice shelf. Geophys. Res. Lett. 44 (19), 9796–9804. https://doi.org/10.1002/2017GL074929.

Gourmelen, N., Escorihuela, M.J., Shepherd, A., Foresta, L., Muir, A., Garcia-Mondejar, A., Roca, M., Baker, S.G., Drinkwater, M.R., 2018. CryoSat-2 swath interferometric altimetry for mapping ice elevation and elevation change. Adv. Space Res. 62 (6), 1226–1242. https://doi.org/10.1016/j.asr.2017.11.014.

Gray, L., Burgess, D., Copland, L., Cullen, R., Galin, N., Hawley, R., Helm, V., 2013. Interferometric swath processing of Cryosat data for glacial ice topography. Cryosphere 7 (6), 1857–1867. https://doi.org/10.5194/tc-7-1857-2013.

Gray, L., Burgess, D., Copland, L., Demuth, M.N., Dunse, T., Langley, K., Schuler, T.V., 2015. CryoSat-2 delivers monthly and inter-annual surface elevation change for Arctic ice caps. Cryosphere 9 (5), 1895–1913. https://doi.org/10.5194/tc-9-1895-2015.

Gray, L., Burgess, D., Copland, L., Dunse, T., Langley, K., Moholdt, G., 2017. A revised calibration of the interferometric mode of the CryoSat-2 radar altimeter improves ice height and height change measurements in western Greenland. Cryosphere 11 (3), 1041–1058. https://doi.org/10.5194/tc-11-1041-2017.

Gray, L., Burgess, D., Copland, L., Langley, K., Gogineni, P., Paden, J., Leuschen, C., van As, D., Fausto, R., Joughin, I., Smith, B., 2019. Measuring height change around the periphery of the Greenland ice sheet with radar altimetry. Front. Earth Sci. 7, 146. https://doi.org/10.3389/feart.2019.00146.

Hawley, R.L., Brandt, O., Dunse, T., Hagen, J.O., Helm, V., Kohler, J., Langley, K., Malnes, E., Høgda, K.A., 2013. Using airborne Ku-band altimeter waveforms to investigate winter accumulation and glacier facies on Austfonna, Svalbard. J. Glaciol. 59 (217), 893–899. https://doi.org/10.3189/2013JoG13J051.

Helm, V., Humbert, A., Miller, H., 2014. Elevation and elevation change of Greenland and Antarctica derived from CryoSat-2. Cryosphere 8 (4), 1539–1559. https://doi.org/10.5194/tc-8-1539-2014.

Hurkmans, R.T.W.L., Bamber, J.L., Griggs, J.A., 2012. Brief communication "Importance of slope-induced error correction in volume change estimates from radar altimetry". Cryosphere 6 (2), 447–451. https://doi.org/10.5194/tc-6-447-2012.

Huss, M., 2013. Density assumptions for converting geodetic glacier volume change to mass change. Cryosphere 7 (3), 877–887. https://doi.org/10.5194/tc-7-877-2013.

Hvidegaard, S.M., Nielsen, J.E., Sandberg Sørensen, L., Simonsen, S.B., Skourup, H., Forsberg, R., Helm, V., Bjerg, T., 2015. ESA CryoVEx 2014-Airborne ASIRAS Radar and Laser Scanner Measurements during 2014 CryoVEx Campaign in the Arctic, Tech. rep. National Space Institute, Technical University of Denmark, Kgs. Lyngby, Denmark.

Jakob, L., Gourmelen, N., Ewart, M., Plummer, S., 2021. Spatially and temporally resolved ice loss in high mountain Asia and the Gulf of Alaska observed by CryoSat-2 swath altimetry between 2010 and 2019. Cryosphere 15 (4), 1845–1862. https://doi.org/10.5194/tc-15-1845-2021.

Lang, C., Fettweis, X., Erpicum, M., 2015. Stable climate and surface mass balance in Svalbard over 1979-2013 despite the Arctic warming. Cryosphere 9 (1), 83–101. https://doi.org/10.5194/tc-9-83-2015.

McMillan, M., Corr, H., Shepherd, A., Ridout, A., Laxon, S., Cullen, R., 2013. Three-dimensional mapping by CryoSat-2 of subglacial lake volume changes. Geophys. Res. Lett. 40 (16), 4321–4327. https://doi.org/10.1002/grl.50689.

McMillan, M., Shepherd, A., Gourmelen, N., Dehecq, A., Leeson, A., Ridout, A., Flament, T., Hogg, A., Gilbert, L., Benham, T., van den Broeke, M., Dowdeswell, J.A., Fettweis, X., Noël, B., Strozzi, T., 2014. Rapid dynamic activation of a marine-based Arctic ice cap. Geophys. Res. Lett. 41 (24), 8902–8909. https://doi.org/10.1002/2014GL062255.

McMillan, M., Shepherd, A., Muir, A., Gaudelli, J., Hogg, A.E., Cullen, R., 2018. Assessment of CryoSat-2 interferometric and non-interferometric SAR altimetry over ice sheets. Adv. Space Res. 62 (6), 1281–1291. https://doi.org/10.1016/j.asr.2017.11.036.

Michel, A., Flament, T., Rémy, F., 2014. Study of the penetration bias of ENVISAT altimeter observations over Antarctica in comparison to ICESat observations. Remote Sens. 6 (10), 9412–9434. https://doi.org/10.3390/rs6109412.

Moholdt, G., Hagen, J.O., Eiken, T., Schuler, T.V., 2010. Geometric changes and mass balance of the Austfonna ice cap, Svalbard. Cryosphere 4 (1), 21–34. https://doi.org/10.5194/tc-4-21-2010.

Moholdt, G., Nuth, C., Hagen, J.O., Kohler, J., 2010. Recent elevation changes of Svalbard glaciers derived from ICESat laser altimetry. Remote Sens. Environ. 114 (11), 2756–2767. https://doi.org/10.1016/j.rse.2010.06.008.

Morris, A., Moholdt, G., Gray, L., 2020. Spread of Svalbard glacier mass loss to Barents Sea margins revealed by CryoSat-2. J. Geophys. Res. Earth Surf. 125 (8) https://doi.org/10.1029/2019JF005357.

Nilsson, J., Gardner, A., Sandberg Sørensen, L., Forsberg, R., 2016. Improved retrieval of land ice topography from CryoSat-2 data and its impact for volume-change estimation of the Greenland ice sheet. Cryosphere 10 (6), 2953–2969. https://doi.org/10.5194/tc-10-2953-2016.

Noël, B., van de Berg, W.J., Lhermitte, S., Wouters, B., Schaffer, N., van den Broeke, M. R., 2018. Six decades of glacial mass loss in the Canadian Arctic Archipelago. J. Geophys. Res. Earth Surf. 123 (6), 1430–1449. https://doi.org/10.1029/2017JF004304.

NPI, 2014. Terrengmodell Svalbard (S0 Terrengmodell). https://doi.org/10.21334/npolar.2014.dce53a47.

Nuth, C., Kohler, J., König, M., von Deschwanden, A., Hagen, J.O., Kääb, A., Moholdt, G., Pettersson, R., 2013. Decadal changes from a multi-temporal glacier inventory of Svalbard. Cryosphere 7 (5), 1603–1621. https://doi.org/10.5194/tc-7-1603-2013.

Østby, T.I., Schuler, T.V., Hagen, J.O., Hock, R., Kohler, J., Reijmer, C.H., 2017. Diagnosing the decline in climatic mass balance of glaciers in Svalbard over 1957-2014. Cryosphere 11 (1), 191–215. https://doi.org/10.5194/tc-11-191-2017.

Paolo, F.S., Fricker, H.A., Padman, L., 2015. Volume loss from Antarctic ice shelves is accelerating. Science 348 (6232), 327–331. https://doi.org/10.1126/science.aaa0940.

Pfeffer, W.T., Arendt, A.A., Bliss, A., Bolch, T., Cogley, J.G., Gardner, A.S., Hagen, J.O., Hock, R., Kaser, G., Kienholz, C., Miles, E.S., Moholdt, G., Mölg, N., Paul, F., Radić, V., Rastner, P., Raup, B.H., Rich, J., Sharp, M.J., 2014. The Randolph consortium, the Randolph Glacier Inventory: a globally complete inventory of glaciers. J. Glaciol. 60 (221), 537–552. https://doi.org/10.3189/2014JoG13J176.

Raper, V., Bamber, J., Krabill, W., 2005. Interpretation of the anomalous growth of Austfonna, Svalbard, a large Arctic ice cap. Ann. Glaciol. 42, 373–379. https://doi.org/10.3189/172756405781812790.

Rignot, E., Echelmeyer, K., Krabill, W., 2001. Penetration depth of interferometric synthetic-aperture radar signals in snow and ice. Geophys. Res. Lett. 28 (18), 3501–3504. https://doi.org/10.1029/2000GL012484.

Sandberg Sørensen, L., Simonsen, S., Langley, K., Gray, L., Helm, V., Nilsson, J., Stenseng, L., Skourup, H., Forsberg, R., Davidson, M., 2018. Validation of CryoSat-2 SARIn data over Austfonna ice cap using airborne laser scanner measurements. Remote Sens. 10 (9), 1354. https://doi.org/10.3390/rs10091354.

Sandberg Sørensen, L., Simonsen, S.B., Forsberg, R., Khvorostovsky, K., Meister, R., Engdahl, M.E., 2018. 25 years of elevation changes of the Greenland ice sheet from ERS, Envisat, and CryoSat-2 radar altimetry. Earth Planet. Sci. Lett. 495, 234–241. https://doi.org/10.1016/j.epsl.2018.05.015.

Scagliola, M., Fornari, M., Bouffard, J., Parrinello, T., 2018. The CryoSat interferometer: end-to-end calibration and achievable performance. Adv. Space Res. 62 (6), 1516–1525. https://doi.org/10.1016/j.asr.2017.09.024.

Schröder, L., Richter, A., Fedorov, D.V., Eberlein, L., Brovkov, E.V., Popov, S.V., Knöfel, C., Horwath, M., Dietrich, R., Matveev, A.Y., Scheinert, M., Lukin, V.V., 2017. Validation of satellite altimetry by kinematic GNSS in central East Antarctica. Cryosphere 11 (3), 1111–1130. https://doi.org/10.5194/tc-11-1111-2017.

Schuler, T.V., Loe, E., Taurisano, A., Eiken, T., Hagen, J.O., Kohler, J., 2007. Calibrating a surface mass-balance model for Austfonna ice cap, Svalbard. Ann. Glaciol. 46, 241–248. https://doi.org/10.3189/172756407782871783.

Schuler, T.V., Dunse, T., Østby, T.I., Hagen, J.O., 2014. Meteorological conditions on an Arctic ice cap-8 years of automatic weather station data from Austfonna, Svalbard. Int. J. Climatol. 34 (6), 2047–2058. https://doi.org/10.1002/joc.3821.

Schuler, T.V., Kohler, J., Elagina, N., Hagen, J.O.M., Hodson, A.J., Jania, J.A., Kääb, A. M., Luks, B., Małecki, J., Moholdt, G., et al., 2020. Reconciling Svalbard glacier mass balance. Front. Earth Sci. 8, 156. https://doi.org/10.3389/feart.2020.00156.

Scott, J.B.T., Nienow, P., Mair, D., Parry, V., Morris, E., Wingham, D.J., 2006. Importance of seasonal and annual layers in controlling backscatter to radar altimeters across the percolation zone of an ice sheet. Geophys. Res. Lett. 33 (24) https://doi.org/10.1029/2006GL027974.

Shepherd, A., Ivins, E.R., Geruo, A., Barletta, V.R., Bentley, M.J., Bettadpur, S., Briggs, K. H., Bromwich, D.H., Forsberg, R., Galin, N., et al., 2012. A reconciled estimate of ice-sheet mass balance. Science 338 (6111), 1183–1189. https://doi.org/10.1126/science.1228102.

Shepherd, A., Ivins, E., Rignot, E., Smith, B., van den Broeke, M., Velicogna, I., Whitehouse, P., Briggs, K., Joughin, I., Krinner, G., et al., 2018. Mass balance of the Antarctic ice sheet from 1992 to 2017. Nature 556 (7709), 219–222. https://doi.org/10.1038/s41586-018-0179-y.

Shepherd, A., Ivins, E., Rignot, E., Smith, B., Van Den Broeke, M., Velicogna, I., Whitehouse, P., Briggs, K., Joughin, I., Krinner, G., et al., 2020. Mass balance of the Greenland ice sheet from 1992 to 2018. Nature 579 (7798), 233–239. https://doi.org/10.1038/s41586-019-1855-2.

Skourup, H., Barletta, V., Einarsson, I., Forsberg, R., Haas, C., Helm, V., Hvidegaard, S. M., Nilsson, J., Sandberg Sørensen, L., 2012. ESA CryoVEx 2011: Airborne Field Campaign with ASIRAS Radar, EM Induction Sounder and Laser Scanner. National Space Institute, Technical University of Denmark, Kgs. Lyngby, Denmark. Tech. rep.

Skourup, H., Einarsson, I., Forsberg, R., Haas, C., Helm, V., Hvidegaard, S.M., Nilsson, J., Olesen, A.V., Olesen, A.K., 2012. ESA CryoVEx 2012: Airborne Field Campaign with ASIRAS Radar, EM Induction Sounder and Laser Scanner, Tech. rep. National Space Institute, Technical University of Denmark, Kgs. Lyngby, Denmark.

Skourup, H., Simonsen, S.B., Sandberg Sørensen, L., Helm, V., Hvidegaard, S.M., Di Bella, A., Forsberg, R., 2018. ESA CryoVEx/EU ICE-ARC 2016-Airborne Field Campaign with ASIRAS Radar and Laser Scanner Over Austfonna, Fram Strait and the Wandel Sea, Tech. rep. National Space Institute, Technical University of Denmark, Kgs. Lyngby, Denmark.

Smith, B.E., Gourmelen, N., Huth, A., Joughin, I., 2017. Connected subglacial lake drainage beneath Thwaites glacier, west Antarctica. Cryosphere 11 (1), 451–467. https://doi.org/10.5194/tc-11-451-2017.

Smith, B., Fricker, H.A., Gardner, A.S., Medley, B., Nilsson, J., Paolo, F.S., Holschuh, N., Adusumilli, S., Brunt, K., Csatho, B., Harbeck, K., Markus, T., Neumann, T., Siegfried, M.R., Zwally, H.J., 2020. Pervasive ice sheet mass loss reflects competing ocean and atmosphere processes. Science 368 (6496), 1239–1242. https://doi.org/10.1126/science.aaz5845.

Strozzi, T., Paul, F., Wiesmann, A., Schellenberger, T., Kääb, A., 2017. Circum-Arctic changes in the flow of glaciers and ice caps from satellite SAR data between the 1990s and 2017. Remote Sens. 9 (9) https://doi.org/10.3390/rs9090947.

Studinger, M., Koenig, L., Martin, S., Sonntag, J., 2010. Operation icebridge: using instrumented aircraft to bridge the observational gap between ICESat and ICESat-2. In: 2010 IEEE International Geoscience and Remote Sensing Symposium. IEEE, pp. 1918–1919. https://doi.org/10.1109/IGARSS.2010.5650555.

Taurisano, A., Schuler, T.V., Hagen, J.O., Eiken, T., Loe, E., Melvold, K., Kohler, J., 2007. The distribution of snow accumulation across the Austfonna ice cap, Svalbard: direct measurements and modelling. Polar Res. 26 (1), 7–13. https://doi.org/10.1111/j.1751-8369.2007.00004.x.

Tepes, P., Nienow, P., Gourmelen, N., 2021. Accelerating ice mass loss across Arctic Russia in response to atmospheric warming, sea ice decline, and Atlantification of the Eurasian Arctic Shelf Seas. J. Geophys. Res. Earth Surf. 126 (7) https://doi.org/10.1029/2021JF006068.

Tepes, P., Gourmelen, N., Nienow, P., Tsamados, M., Shepherd, A., Weissgerber, F., 2021. Changes in elevation and mass of Arctic glaciers and ice caps, 2010-2017. Remote Sens. Environ. 261, 112481. https://doi.org/10.1016/j.rse.2021.112481.

Wingham, D.J., Francis, C.R., Baker, S., Bouzinac, C., Brockley, D., Cullen, R., de Chateau-Thierry, P., Laxon, S.W., Mallow, U., Mavrocordatos, C., Phalippou, L., Ratier, G., Rey, L., Rostan, F., Viau, P., Wallis, D.W., 2006. CryoSat: a mission to determine the fluctuations in Earth's land and marine ice fields. Adv. Space Res. 37 (4), 841–871. https://doi.org/10.1016/j.asr.2005.07.027.

Wouters, B., Martin-Español, A., Helm, V., Flament, T., van Wessem, J.M., Ligtenberg, S. R.M., van den Broeke, M.R., Bamber, J.L., 2015. Dynamic thinning of glaciers on the southern Antarctic Peninsula. Science 348 (6237), 899–903. https://doi.org/10.1126/science.aaa5727.

Wouters, B., Gardner, A.S., Moholdt, G., 2019. Global glacier mass loss during the GRACE satellite mission (2002-2016). Front. Earth Sci. 7, 96. https://doi.org/10.3389/feart.2019.00096.

Zwally, H.J., Giovinetto, M.B., Li, J., Cornejo, H.G., Beckley, M.A., Brenner, A.C., Saba, J. L., Yi, D., 2005. Mass changes of the Greenland and Antarctic ice sheets and shelves and contributions to sea-level rise: 1992-2002. J. Glaciol. 51 (175), 509–527. https://doi.org/10.3189/172756505781829007.